

# 1 **Seismo-acoustic and GNSS observations of a record-breaking Black** 2 **Sea storm: repurposing geophysical sensors for environmental** 3 **monitoring**

4  
5 Laura Petrescu<sup>1,2,\*</sup>, Bogdan Antonescu<sup>1,2</sup>, Sorin Nistor<sup>3</sup>, Iustin Floroiu<sup>4,5</sup>, Dragoş Ene<sup>1</sup>, Daniela  
6 Ghica<sup>1</sup>, Constantin Ionescu<sup>1</sup>, Andrei Anghel<sup>4</sup>, Mihai Datcu<sup>4</sup>

- 7  
8 1. National Institute for Earth Physics, Magurele, Romania  
9 2. University of Bucharest, Faculty of Physics, Magurele, Romania  
10 3. University of Oradea, Faculty of Construction, Cadaster and Architecture, Oradea,  
11 Romania  
12 4. Politehnica University of Bucharest, Faculty of Electronics, Telecommunications and  
13 Information Technology, Bucharest, Romania  
14 5. Politehnica University of Bucharest, Doctoral School of Electronics,  
15 Telecommunications & Information Technology, Bucharest, Romania

16  
17 \* [laura.petrescu@infp.ro](mailto:laura.petrescu@infp.ro)

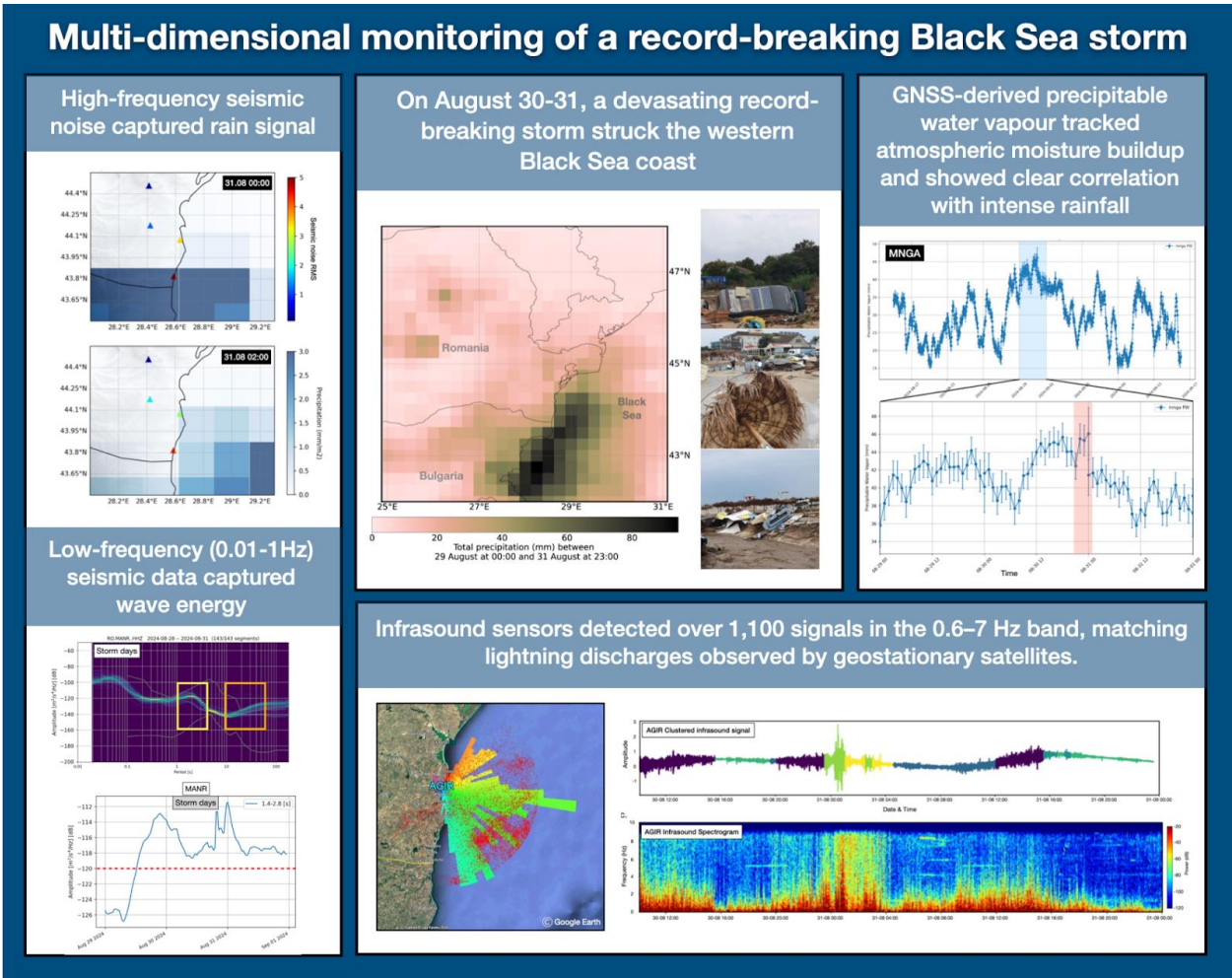
## 18 19 **Abstract**

20  
21 In August 2024, a devastating storm struck Romania’s Black Sea coast, setting new precipitation  
22 records and highlighting the increasing frequency of extreme weather events. This study explores  
23 the integration of non-conventional sensors (seismic, GNSS, infrasound, and satellite data) with  
24 ERA5 meteorological reanalysis to monitor storm dynamics. High-frequency (>30 Hz) seismic  
25 signals captured precipitation, while microseismic bands (0.1-1Hz) reflected wave-induced ground  
26 motion. Analysis of infrasound data via unsupervised learning delineated periods of acoustic  
27 quiescence from storm-related activity. The temporal evolution of these infrasound states  
28 coincided with distinct patterns in seismic ground motion, suggesting a shared origin in the storm's  
29 atmospheric dynamics. The infrasound array also detected over 1,100 signals in the 0.6-7 Hz band,  
30 matching lightning discharges observed by geostationary satellites. GNSS data recorded a buildup  
31 of precipitable water vapor that peaked concurrently with intense rainfall, following a multi-day  
32 increase that preceded the main storm phase. This study highlights the value of integrating diverse,  
33 non-traditional datasets to enhance the resolution and depth of storm analysis. Their combined use  
34 offers a more holistic understanding of storm evolution and supports future research on the  
35 potential role of multi-sensor observations in improving early-warning systems in vulnerable  
36 coastal regions.

37

38 **Graphical abstract**

39



40

41

42

43

44

45

46

47

## 48 **1. Introduction**

49 Climate change has become a critical global issue, with far-reaching effects on weather patterns  
50 and the frequency and intensity of extreme events (Stott, 2016). These changes are not only  
51 contributing to more severe weather events but also altering the timing, location, and duration of  
52 storms, making them harder to predict and manage (Bengtsson et al., 2006). Understanding how  
53 to effectively monitor and predict the behavior of storms, particularly extreme ones, is crucial for  
54 improving forecasting models, enhancing early warning systems, and mitigating their impacts on  
55 both natural and human systems.

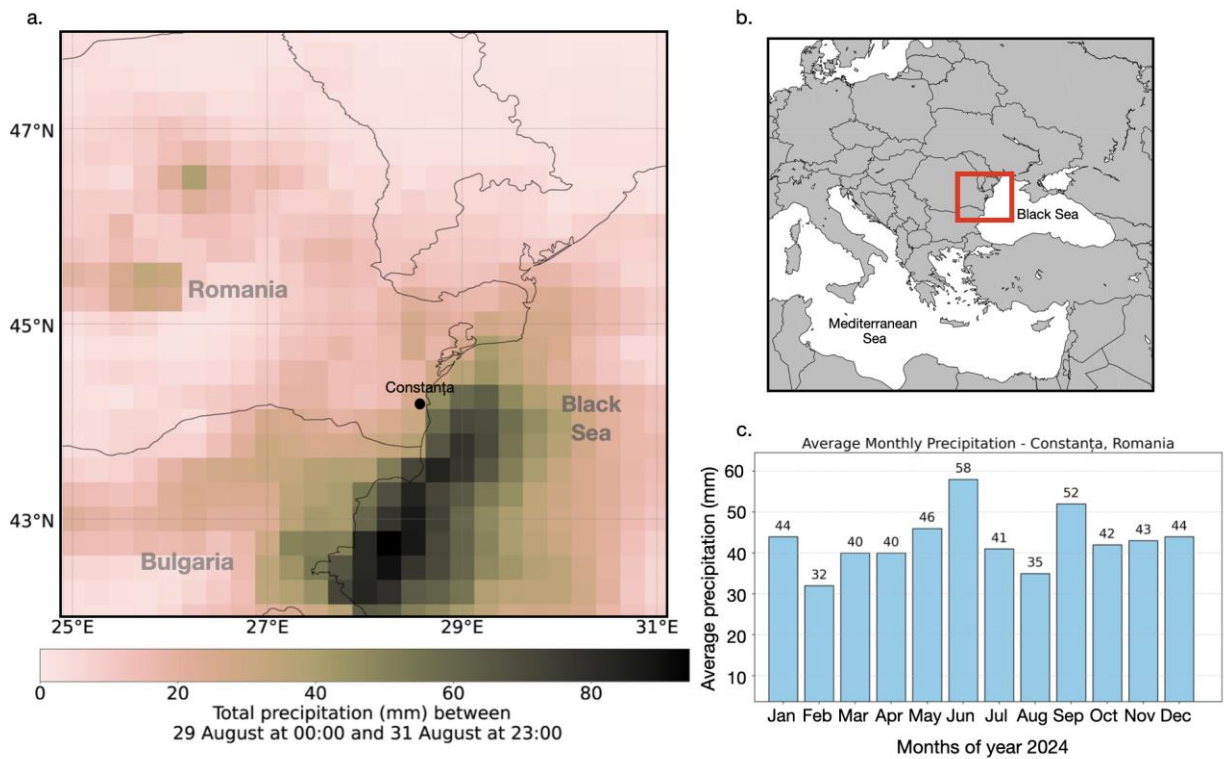
56 Traditional meteorological monitoring relies heavily on ground-based stations, weather radars, and  
57 satellite observations to track and predict storm behavior (Kober and Tafferner, 2009). These  
58 systems have been the backbone of weather forecasting for decades, providing valuable data on  
59 temperature, pressure, wind speed, and precipitation. However, while these methods are effective,  
60 they often have limitations in terms of spatial coverage (e.g. Sokol et al., 2021), particularly in  
61 remote or hard-to-reach areas. Additionally, they may struggle to capture certain atmospheric  
62 phenomena in real-time. As a result, non-conventional monitoring methods are increasingly being  
63 integrated into storm tracking efforts to complement existing meteorological approaches (e.g. Bosity  
64 et al., 2012; Burtin et al., 2016; Diaz et al., 2023; Coviello et al., 2024).

65 In this context, our study focuses on the integration of alternative environmental datasets, including  
66 GNSS stations, infrasound sensors, and seismic data, to track the dynamics of an extreme storm  
67 event, as part of a national climate change resilience strategy, implemented through the DTE  
68 Climate project (<https://dteclimate.upb.ro/>). GNSS data provide valuable information on  
69 atmospheric water vapor, helping to track moisture changes that influence storm formation and  
70 intensity (Bosity et al, 2012; Marut et al., 2022). Infrasound sensors detect low-frequency acoustic  
71 waves generated by storm activity, such as lightning or large-scale weather system movements  
72 like microbaroms (e.g. Landès et al., 2012). Seismic data, though traditionally used for earthquake  
73 monitoring, can also record vibrations caused by storm-induced pressure changes, making it useful  
74 for detecting rainstorms, floods, or tropical cyclones (e.g. Retailleau and Gualtieri, 2021). Through  
75 the integration of these diverse sensor networks, our work highlights their synergy in improving  
76 storm detection, monitoring capabilities, and, potentially, early warning systems, contributing to  
77 more robust climate resilience strategies.

## 78 **2. Study area and storm overview**

79  
80 The Black Sea region (Figure 1) is characterized by a unique combination of geographic and  
81 meteorological features that significantly influence its climate and weather patterns. Nestled  
82 between Europe and Asia, the Black Sea is bordered by six countries with diverse landscapes, from  
83 mountainous areas to flat plains. This geography, combined with the Black Sea's relatively shallow  
84 waters compared to oceanic environments and its connection to the Mediterranean through the  
85 Bosphorus Strait, creates an environment where rapid changes in weather are common.  
86 Understanding the dynamics of these extreme weather events is crucial, as they can have a  
87 profound impact on the environment, economy, and daily life in the region. Monitoring such events  
88 is key to improving our ability to predict their occurrence and intensity. By studying the complex  
89 atmospheric processes that govern these storms, we can enhance predictive models and refine early

90 warning systems, ultimately helping to mitigate the risks and protect the communities and  
91 ecosystems most vulnerable to these extreme weather phenomena.



92  
93 *Figure 1. a. Total precipitation accumulated (in mm, shaded according to the scale) between 29*  
94 *August 00 UTC and 31 August 23:00 UTC extracted from ERA5 data. b. Map of Europe with red*  
95 *square marking the study region; c. Average monthly precipitation rates in Constanța, Romania.*

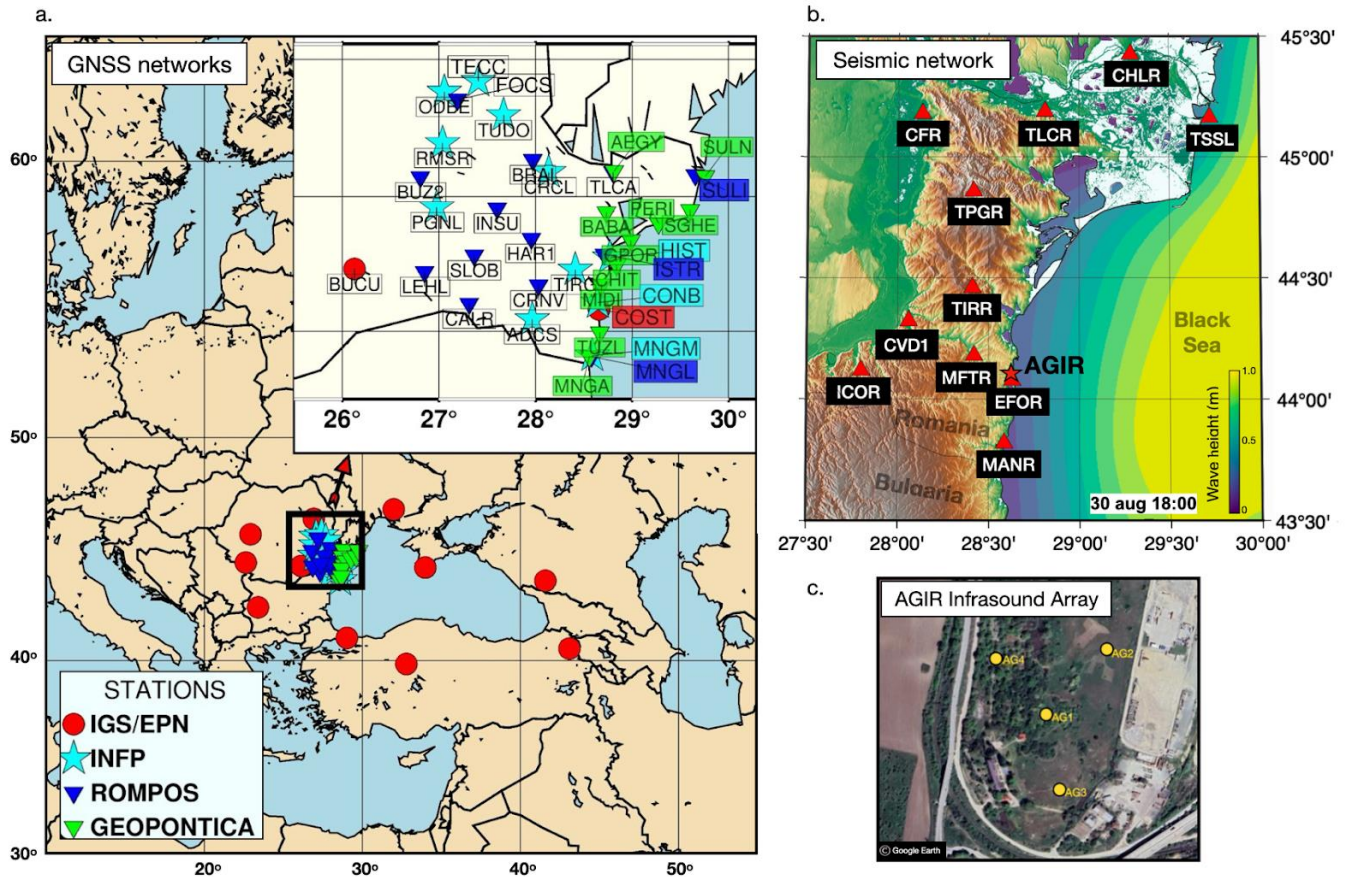
96 In August 2024, Romania experienced severe flooding, largely driven by a storm that brought  
97 unusual precipitation patterns to the Black Sea coastal region. Exceptional precipitation totals were  
98 recorded over south-eastern Romania in particular in Mangalia (234.7 mm), Agigea (145 mm),  
99 and Tuzla (118 mm), leading to significant flooding in coastal towns (Figure 1). Over 800  
100 emergency calls prompted large-scale intervention by ISU Dobrogea, focusing on evacuations,  
101 debris clearance, and infrastructure restoration (Antonescu et al. 2024). According to the National  
102 Meteorological Agency official records ([https://www.meteoromania.ro/clim/caracterizare-](https://www.meteoromania.ro/clim/caracterizare-lunara/cc_2024_08.html)  
103 [lunara/cc\\_2024\\_08.html](https://www.meteoromania.ro/clim/caracterizare-lunara/cc_2024_08.html)), one of the coastal stations at Mangalia, recorded a total of 343.6 mm of  
104 precipitation in August 2024, breaking the previous record of 159.1 mm from 1947, and  
105 significantly surpassing the average monthly precipitation values for this area (Figure 1c). A  
106 remarkable 234.7 mm of this total fell in a single day on August 31, 2024, highlighting the event's  
107 exceptional intensity.

108 An analysis conducted by ClimaMeter ([www.climameter.org](http://www.climameter.org), Faranda et al. 2024, Antonescu et  
109 al. 2024) immediately after the event, showed that low pressure systems similar to the one that  
110 caused the floods typically result in reduced rainfall (7 mm day<sup>-1</sup>, or up to 15% less) in eastern  
111 Romania compared to historical trends. However, this particular storm led to a significant local  
112 increase in precipitation, particularly in Constanța, one of the coastal cities severely affected by

113 the flooding. In Constanța, daily rainfall reached up to 5 mm day<sup>-1</sup>, or up to 10% more than usual,  
114 marking a notable deviation from the region’s typical weather behavior. The changes in  
115 precipitation that contributed to the flooding are largely attributed to human-induced climate  
116 change, with natural climate variability likely playing a modest role. As climate change continues  
117 to influence weather patterns, understanding the connection between changing precipitation levels  
118 and extreme weather events like flooding is crucial for improving forecasting and resilience in the  
119 face of such disasters.

### 120 **3. Data and Methods**

121 The analysis of the storm event integrates a variety of data sources and methodologies to provide  
122 a comprehensive understanding of its dynamics. Seismic data, infrasound measurements, GNSS  
123 water vapor data, and ERA5 reanalysis data are all utilized to capture different aspects of the  
124 storm’s behavior (Figure 2). Seismic data offers insights into ground vibrations and atmospheric  
125 disturbances, while infrasound monitoring detects low-frequency acoustic signals generated by  
126 lightning and other meteorological phenomena. GNSS water vapor data provides valuable  
127 information on atmospheric moisture. Additionally, ERA5 reanalysis data (Hersbach et al. 2020),  
128 which provides detailed atmospheric and wave dynamics data, helps contextualize the storm's  
129 impact within broader weather patterns. Together, these diverse data sources enable a multifaceted  
130 approach to studying the storm and its effects.



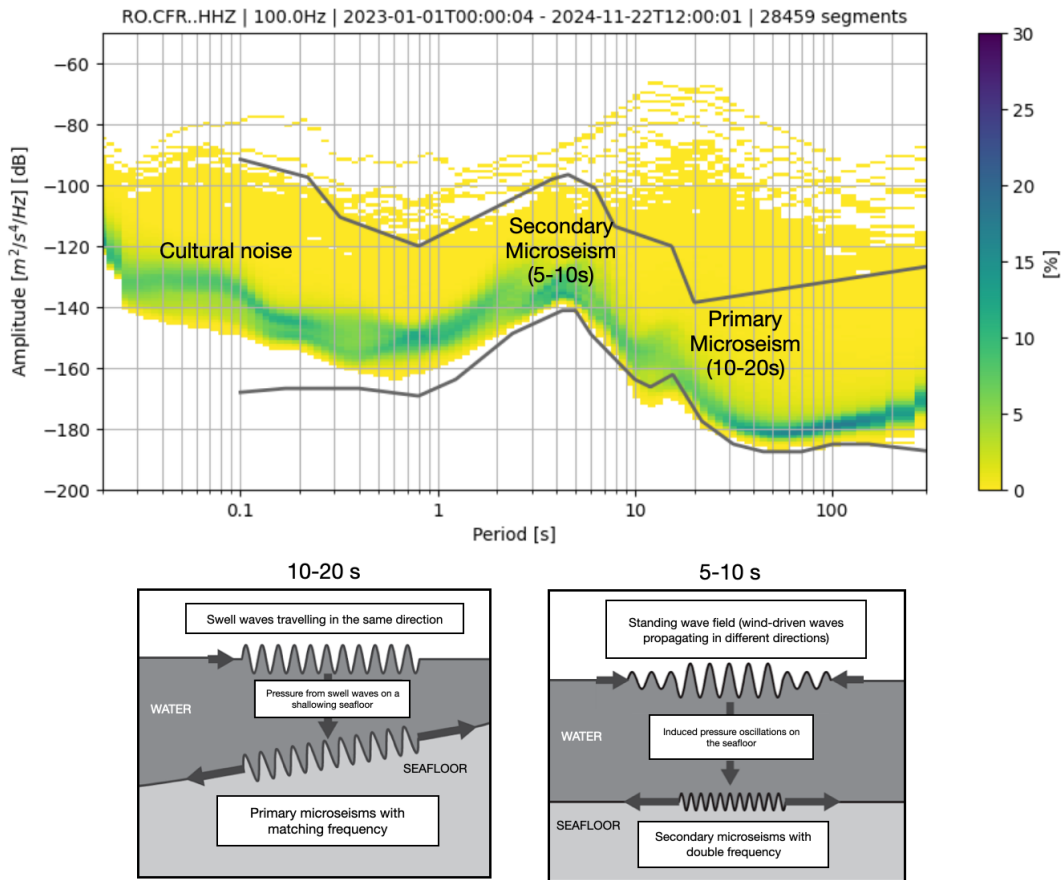
131  
 132 *Figure 2. a. Map of Europe and the Black Sea coast showing GNSS stations and their belonging networks*  
 133 *used for analysis in this study. b. Map of the Romanian sea coast showing seismic stations (red triangles)*  
 134 *and the location of the AGIR infrasound array (star). Coloured contours represent total wave height at*  
 135 *18:00 UTC on the 30th of August 2024 from ERA5 reanalysis data. c. The layout of the AGIR infrasound*  
 136 *array.*

137  
 138 **3.1 Seismic Data**

139 Seismic data represents vibrations of the Earth's surface, commonly referred to as seismic noise.  
 140 These low-amplitude movements are recorded across the Earth's surface and are traditionally used  
 141 to study the Earth's internal structure and detect earthquakes. Recently, it has increasingly found  
 142 applications in meteorology and hydrology, particularly for monitoring weather events (e.g. Dias  
 143 et al. 2023; Hua et al., 2023), destructive flood episodes (Burtin et al., 2016), ocean storms, and  
 144 tropical cyclones (Gualtieri et al., 2018). Seismic noise can reveal the impact of atmospheric and  
 145 oceanic conditions, providing valuable insights into weather events and climate changes (e.g.  
 146 Bromirski et al., 2002; Aster et al, 2008; 2023). In particular, seismic data helps track variations  
 147 in the Earth's surface caused by factors such as ocean waves, wind, and precipitation, offering a  
 148 unique perspective on these phenomena (e.g. Grevemeyer et al., 2000; Borzi et al., 2022).

149 When the seismic noise is analyzed in the frequency domain, two clear peaks emerge in the  
 150 spectrum (Figure 3), reflecting distinct types of ocean wave interactions (Koper et al., 2015;

151 Arduin et al., 2019; Tanimoto et al., 2023). The primary peak, observed in the range of 10-20  
 152 seconds (0.05-1 Hz), is generated by the impact of "swell" waves traveling in the same direction,  
 153 inducing pressure variations in the Earth's crust that match the period of the waves. The secondary  
 154 peak, in the range of 5-10 seconds (0.1-0.5 Hz), is produced by wind-driven waves, which  
 155 propagate in different directions and generate pressure oscillations on the ocean floor (Ebeling et  
 156 al., 2012). These seismic signals directly link ocean conditions with seismic activity (Li et al.,  
 157 2020), providing insights into large-scale weather phenomena like ocean storms.



158

159 *Figure 3. Probabilistic Power Spectral Density (PPSD) of seismic noise for station CFR, over two years,*  
 160 *showing key sources of primary and secondary microseisms. Below, sketches illustrate the generation*  
 161 *mechanisms: primary microseisms are caused by unidirectional swell waves inducing pressure fluctuations*  
 162 *on a shoaling seafloor, while secondary microseisms result from nonlinear interactions of wind-driven*  
 163 *waves over deeper water (modified after Ebeling, 2012).*

164 Higher frequencies above 30 Hz are associated with the effects of precipitation and wind, as seen  
 165 in studies like Rindraharisaona et al. (2022) or Diaz et al. (2023). These higher-frequency seismic  
 166 signals help track more localized weather events, such as storms and heavy rainfall. Seismic data,  
 167 when integrated with other meteorological tools, enhances the ability to monitor and predict  
 168 weather events.

169 To analyse seismic data, the raw traces are first corrected for instrument response and converted  
170 to units of velocity. These are then filtered with bandpass butterworth filters adapted to capture the  
171 target signal: low pass filtering (<1 Hz) for wave-seafloor coupled interactions and high pass  
172 filtering (>30 Hz) to identify possible signatures of precipitation, essentially induced pressure  
173 fluctuations in the ground converted to weak seismic vibrations due to rain drops. Spectrograms  
174 of these filtered seismic traces were computed using short-time Fourier transforms implemented  
175 in the `scipy.signal` package, with the default 256-sample window length used for each segment,-to  
176 visualise signatures of the hydro-meteorological phenomena in the frequency content of ground  
177 vibrations.

178 Potential environmental signals in the seismic data were also investigated using power spectral  
179 density (PSD) analysis. To account for variations over time, a Probabilistic Power Spectral Density  
180 (PPSD) method was applied. The continuous waveform was divided into 1-hour time windows  
181 with 50% overlap, and a PSD was computed for each window after instrument-response correction  
182 and basic preprocessing. These estimates were combined into a probability distribution, providing  
183 a statistical overview of typical and transient noise levels across frequencies. The PPSD was  
184 produced using ObsPy (Beyreuther et al., 2010), which handles data gaps and ensures reliable  
185 normalization.

186 Temporal variations in PSD amplitudes are also analyzed to track changes in seismic noise at  
187 specific frequencies. By extracting PSD values at selected frequencies that are expected to capture  
188 primary and secondary microseisms, time series of noise levels are generated. These temporal  
189 PSDs allow for the identification of trends and correlations with environmental factors, such as  
190 ocean wave activity or weather conditions.

### 191 **3.2 Acoustic Data**

192 Infrasound waves are low-frequency acoustic waves that are inaudible to the human ear, typically  
193 below 20 Hz. These waves are generated by a variety of natural and anthropogenic sources,  
194 including meteorological events, volcanic eruptions, earthquakes, and human activities such as  
195 explosions and industrial processes (Campus and Christie, 2009; Bondár et al., 2022). In particular,  
196 infrasound is often associated with phenomena like thunderstorms, ocean waves, and large-scale  
197 atmospheric events, which generate pressure fluctuations that propagate through the atmosphere  
198 (e.g. Stopa et al., 2012; Landès et al., 2012; Listowski et al., 2022). These waves provide valuable  
199 information about the dynamics of weather systems (e.g. Hupe et al., 2019), making them an  
200 essential tool for monitoring and understanding environmental processes (e.g. Brachet et al., 2009;  
201 Hupe et al., 2022). Infrasound associated with thunderstorms, primarily generated by acoustic  
202 waves from thunder, has been studied previously and shown to be detectable at distances ranging  
203 from tens to hundreds of kilometers (e.g., Assink et al., 2008; Sindelarova et al., 2015; Šindelářová  
204 et al., 2021). Nevertheless, infrasound arrays detect signals from multiple storm-related sources,  
205 not just thunder (e.g., Waxler et al., 2024). In the present study, we build on this understanding by  
206 integrating these signals with seismic, satellite, meteorological, and water vapor observations to  
207 investigate what these complementary datasets reveal about storm evolution in a coastal  
208 environment.

209 For the monitoring of infrasound signals, we use data from an infrasound array system located at  
210 Eforie Nord-Agigea, Romania (AGIR, Figure 2). This array consists of multiple sensors, including

211 SIS-1 infrasonic sensors (Seismowave), equipped with global positioning systems (GPS) and noise  
212 reduction technology.

213 To analyze the seismo-acoustic characteristics of the August 30-31 Black Sea storm, we used a  
214 two-pronged approach: (1) single sensor signal analysis based on feature extraction and  
215 unsupervised machine learning, and (2) array-based analysis using all the sensors of AGIR and  
216 classic multi-channel correlation algorithms. Together, these methods provide complementary  
217 insights into the acoustic behavior of the storm, capturing both local signal characteristics and  
218 spatial coherence across sensors.

219 For the single-station analysis, infrasound data recorded at the AGIR sensor (Figure 2) was  
220 segmented into 30-minute windows, and a set of time-frequency features was extracted to  
221 characterize the signal dynamics (Supplementary Material). These features describe how energy  
222 and frequency content evolve over time, providing insights into the structure of the infrasound  
223 signal. Parameters such as spectral centroid and spectral rolloff are standard descriptors in acoustic  
224 signal analysis and are suitable here because they effectively capture shifts in dominant frequency  
225 produced by lightning-generated acoustic waves or the passage of pressure disturbances, while  
226 spectral flux highlights changes in broadband acoustic energy (Pásztor et al., 2023). Spectral  
227 entropy reflects the complexity of the frequency distribution, which increases during turbulent  
228 atmospheric conditions, and the zero-crossing rate, mean, and variance of the power spectrum  
229 summarize overall activity and variability. This feature set provides a compact representation of  
230 the signal suitable for unsupervised machine-learning approaches such as clustering, techniques  
231 widely used in data mining to identify patterns in multidimensional time-frequency data (e.g.,  
232 Coates and Ng, 2012), and allows us to distinguish physically interpretable stages of storm-induced  
233 changes in the infrasound wavefield.

234 The extracted features were used as input for K-Means clustering (MacQueen, 1967), an  
235 unsupervised machine learning algorithm that partitions data into a predefined number of groups.  
236 K-Means minimizes within-cluster variance by iteratively assigning feature vectors to the nearest  
237 cluster centroid and updating the centroids based on the grouped data. This clustering method  
238 enables the identification of distinct acoustic patterns in the signal (e.g. Pásztor et al., 2023),  
239 offering a data-driven way to segment the storm’s infrasound profile without requiring prior labels  
240 or assumptions. Prior to clustering, the features were standardized using z-score normalization, to  
241 ensure comparable scaling across variables. The optimal number of clusters was determined using  
242 the elbow method, which evaluates within-cluster variance as a function of cluster number  
243 (Supplementary Material). To select the most informative features, we applied covariance pruning,  
244 and the temporal evolution of the features was visualized to ensure meaningful representation. This  
245 procedure resulted in six clusters, providing a balanced representation of the infrasound dynamics  
246 while avoiding over-segmentation or overfitting. By combining multiple features in the clustering,  
247 this method captures the evolving acoustic states of the storm in a compact, interpretable form.

248 In parallel with the single-station analysis, we also applied the Progressive Multi-Channel  
249 Correlation (PMCC) method, as implemented in the DTK-PMCC software (Cansi and Le Pichon,  
250 2008; Le Pichon et al., 2010) to detect and analyze coherent acoustic signals across an infrasound  
251 array. The PMCC method targets signals generated by atmospheric sources such as lightning (i.e.,  
252 associated thunders) or other pressure disturbances, operating in the low-frequency range of 0.7 to

253 7 Hz. It is specifically suited for mini-array configurations, where signal coherence between  
254 closely spaced sensors can be exploited for precise signal detection and characterization.

255 The PMCC algorithm was implemented using a multi-resolution configuration following the  
256 standardization proposed by Garcés (2013), with window lengths and frequency bands arranged  
257 in third-octave bands. A total of 19 frequency bands were used, covering 0.1-7 Hz. Window  
258 lengths decrease logarithmically with frequency, ranging from 258 s in the lowest band to 4 s in  
259 the highest band. A 10% time step was applied (corresponding to 90% overlap between  
260 consecutive windows), and this scheme repeats every decade. Within each time-frequency  
261 segment, cross-correlations are computed between all sensor pairs to identify coherent wavefronts,  
262 signals that exhibit consistent arrival times across the array. From these detections, PMCC  
263 estimates several key propagation parameters, including backazimuth (the direction of arrival),  
264 horizontal trace velocity, amplitude, duration, and dominant frequency. This approach is  
265 particularly effective in noisy environments and enables the discrimination of storm-generated  
266 infrasound from background signals or unrelated acoustic sources. The algorithm's output consists  
267 of a time-frequency map of signal detections enriched with physical metadata, allowing for  
268 detailed interpretation of the storm's acoustic footprint and its temporal evolution.

### 269 3.3 Satellite Observations

270 We also incorporated data from the Meteosat Third Generation (MTG) satellite system (Holmlund  
271 et al., 2021), specifically from its Lightning Imager (LI) sensor (Viticchie et al., 2020). The MTG  
272 satellites operate in geostationary orbit at approximately 36,000 km altitude, providing continuous  
273 observations over Europe, Africa, and surrounding waters. The Lightning Imager detects cloud-  
274 to-cloud, cloud-to-ground, and intra-cloud lightning flashes using four cameras that collectively  
275 cover 86% of the Earth's visible disc from the satellite's perspective.

276 For this study, we used Level 2 group data, which includes the geographical coordinates and timing  
277 of each detected flash. The MTG Lightning Imager detects total lightning (cloud-to-cloud and  
278 cloud-to-ground) optically at 777 nm, with 4.5 km pixel resolution at the sub-satellite point and  
279 1 ms frame rate (Holmlund et al., 2021; Kokou, 2023). Level-2 achieves detection efficiencies of  
280 ~80-90%, capturing even weak flashes reliably, with false alarm rates <0.3 (Enno et al., 2025).  
281 Flash geolocation uncertainty reaches 5-10 km near the edge of the instrument's field of view,  
282 where off-nadir viewing geometry amplifies parallax effects (Bližňák & Sokol, 2026). By mapping  
283 these detections, we were able to analyze the spatial distribution and temporal evolution of the  
284 storm's lightning activity. The dataset also offered insights into the storm's intensity and structure,  
285 complementing other meteorological observations.

286 Associations between infrasound detections and lightning flashes detected by MTG within 50 km  
287 of the AGIR infrasound station were investigated by assuming direct-path acoustic propagation  
288 and a correspondence between infrasound time-of-arrival and the MTG lightning discharge time  
289 (after Assink et al., 2008):

$$290 t = t_{\text{MTG}} + d/c + \Delta t,$$

291 where  $d$  is the distance between the lightning discharge and the infrasound station,  $c = 340\text{m/s}$ ,  
292 and  $\Delta t = \pm 10\text{s}$  accounts for timing uncertainty associated with the simplified propagation

293 assumption. In particular, infrasound travel time from thunder sources can vary due to atmospheric  
294 temperature and wind variations along the propagation path, which affect the effective sound speed  
295 and may introduce deviations from the assumed constant-velocity, straight-path propagation.  
296 Additionally, a maximum angular deviation of  $10^\circ$  between the observed infrasound backazimuth  
297 and the MTG-derived backazimuth is permitted for an association to be accepted.

### 298 **3.4 GNSS Data**

299 The use of GNSS technology for atmospheric monitoring provides a powerful tool for analyzing  
300 extreme weather events. Beyond its well-known applications in navigation and timing, GNSS has  
301 become a reliable method for sensing tropospheric water vapour, an essential driver of weather  
302 systems and a key variable in forecasting models (Guerova et al., 2016; Vaquero-Martínez and  
303 Antón, 2021). Over the past two decades, ground-based GNSS networks in Europe have  
304 contributed significantly to operational meteorology by providing near real-time estimates of  
305 atmospheric water vapour, aiding in the detection and tracking of severe weather, including heavy  
306 rainfall and storms (Karabatić et al., 2011; Priego et al., 2017; Jones et al., 2020). These high-  
307 resolution observations have proven valuable for both nowcasting and validating numerical  
308 weather prediction models (Wilgan et al., 2015; Bosy et al., 2012; Awange, 2012).

309 In this study, GNSS data were collected from several networks (Figure 2), including the  
310 International GNSS Service (IGS, Johnston et al., 2017), the EUREF Permanent Network (EPN,  
311 Bruyninx et al., 2012), the Romanian Position Determination System (ROMPOS, Iliescu et al.,  
312 2019), and GEOPONTICA (Dimitriu et al., 2017). A total of 37 permanent GNSS stations were  
313 analyzed over a 30-day period, with the rainiest interval selected at the midpoint of the study  
314 period. These stations provide high-quality, continuous observations critical for atmospheric  
315 monitoring.

316 The data were processed using a double-differenced, ionosphere-free combination of L1 and L2  
317 carrier phases. This approach helps minimize errors such as ionospheric delays, satellite clock  
318 biases, and other common atmospheric effects. The resulting Zenith Tropospheric Delay (ZTD)  
319 values were then corrected using the Vienna Mapping Functions 3 (VMF3, Landskron et al., 2018),  
320 which improves the accuracy of ZTD by accounting for variations in the troposphere's atmospheric  
321 conditions. Once the ZTD was refined, it was converted into integrated precipitable water vapor  
322 (PWV) using surface meteorological data (temperature and pressure) from co-located weather  
323 stations, following the method outlined by Bosy et al. (2012). This process allowed for the  
324 derivation of high-resolution atmospheric water vapor content, critical for analyzing the dynamics  
325 of the extreme storm event over the Black Sea. By combining GNSS-derived PWV with data from  
326 other observational sources, the study captured the temporal and spatial variations in atmospheric  
327 moisture, offering valuable insights into the storm's development and intensity.

### 328 **3.5 Meteorological Data**

329 To compare the infrasound signals captured during the Black Sea extreme storm event, we  
330 extracted meteorological data from the open-access ERA5 reanalysis dataset, produced by the  
331 European Centre for Medium-Range Weather Forecasts (ECMWF). This dataset provides a  
332 comprehensive record of global weather conditions from 1950 to the present (Hersbach et al.,  
333 2023). ERA5 combines observational data and advanced numerical models to generate relatively

334 high-resolution atmospheric parameters compared with earlier global reanalyses, including  
335 precipitation (Figure 1), wind speed, and wave height. ERA5 has been extensively validated (Jiao  
336 et al., 2021; Wu et al., 2022; Soci et al., 2024) and is widely used in studies of storm evolution and  
337 precipitation dynamics (e.g. Dullart et al., 2020; Tiberia et al., 2021; Price et al., 2025), making it  
338 a suitable choice for the mesoscale processes examined here.

339 For our study, the ERA5 data was used to track the meteorological context of the storm, offering  
340 insights into the intensity of precipitation, the evolution of wind patterns, and the development of  
341 oceanic wave heights. With a temporal resolution of 1 hour and spatial resolution of  $0.25^\circ \times 0.25^\circ$ ,  
342 ERA5 allows for a mesoscale comparison of the storm's meteorological characteristics over time.  
343 While its spatial averaging cannot resolve localized convective-scale precipitation, it provides a  
344 vital benchmark for qualitative comparisons and for testing multi-sensor monitoring potential.  
345 These comparisons help us understand the storm's dynamics and assess its impact, further  
346 enhancing the interpretation of infrasound signals and aiding in future storm prediction and  
347 monitoring efforts. The open-access nature of ERA5 ensures broad accessibility, contributing to  
348 the transparency and reproducibility of our storm analysis (Copernicus Climate Change Service,  
349 Climate Data Store, 2023).

## 350 **4. Results**

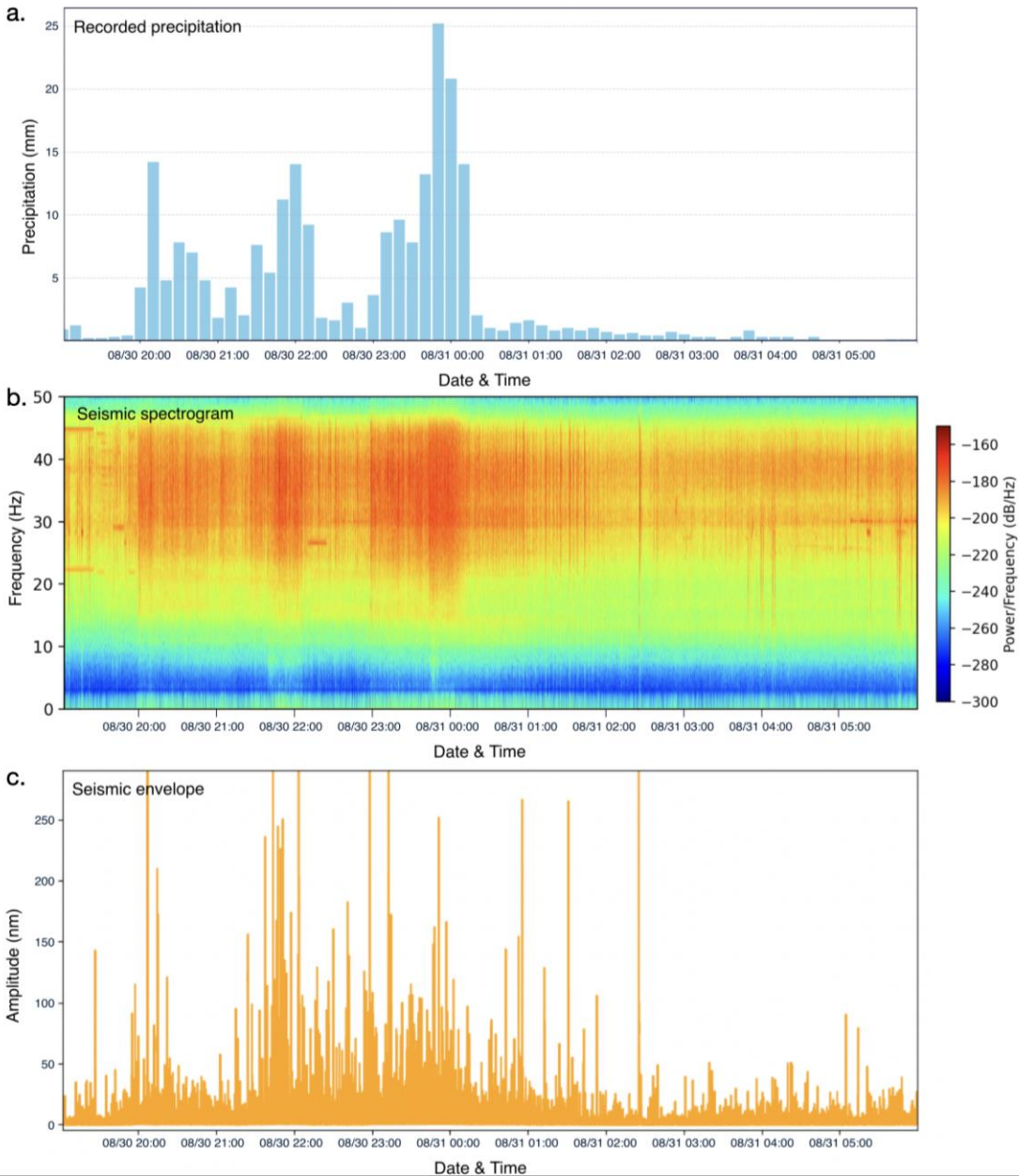
### 351 **4.1 Seismic signatures of storm evolution**

352 High frequency ( $>30$  Hz) analysis of seismic noise reveals strong signals during periods of intense  
353 rainfall (Figure 4). Specifically, the displacement envelope at station MANR and its spectrogram  
354 for 30 August, 12:00 UTC to 31 August, 06:00 UTC (Figures 4b, c) reveal strong signal around  
355 midnight, when recorded precipitation exceeded 20 mm per 10 minutes. Similar temporal patterns  
356 in the seismic spectrogram were also visible when compared with hourly precipitation levels from  
357 ERA5, indicating that the high amplitude of energy observed above 30 Hz is most plausibly  
358 generated by raindrop impacts.

359 However, this correspondence is not uniform across all rainfall episodes. While the main  
360 precipitation maximum on 30-31 August produces a clear and sustained seismic response, several  
361 lower-intensity precipitation pulses show a much weaker or no recognizable signature in either the  
362 seismic envelope or spectrogram. This behaviour is consistent with previous work (e.g.,  
363 Rindraharisaona et al., 2022), which demonstrates that only rainfall above a certain intensity, or  
364 involving sufficiently large drops, generates impact forces strong enough to be detected by  
365 broadband seismometers. Our observations therefore reflect both strong positive correlations  
366 during intense rainfall and the lack of seismic expression for weaker precipitation. This selective  
367 sensitivity supports the interpretation that high-frequency seismic noise can reflect strong rainfall  
368 peaks but is less responsive to light or moderate precipitation, an important nuance when  
369 interpreting multi-sensor relationships in this study.

370 Anthropogenic seismic noise is typically strongest at low to mid frequencies ( $<25$  Hz), where day-  
371 night variations reflect traffic, human activity, and transient signals from machinery, while higher-  
372 frequency bands (25-45 Hz) may include periodic contributions from rotating equipment (e.g.,  
373 Gross & Ritter, 2008; Diaz et al., 2017). The bandwidth targeting rainfall in this case is between

374 30-50 Hz, which is above the dominant frequency content of most anthropogenic sources and  
375 overlaps with raindrop-impact energy documented in recent rainfall-seismic studies.

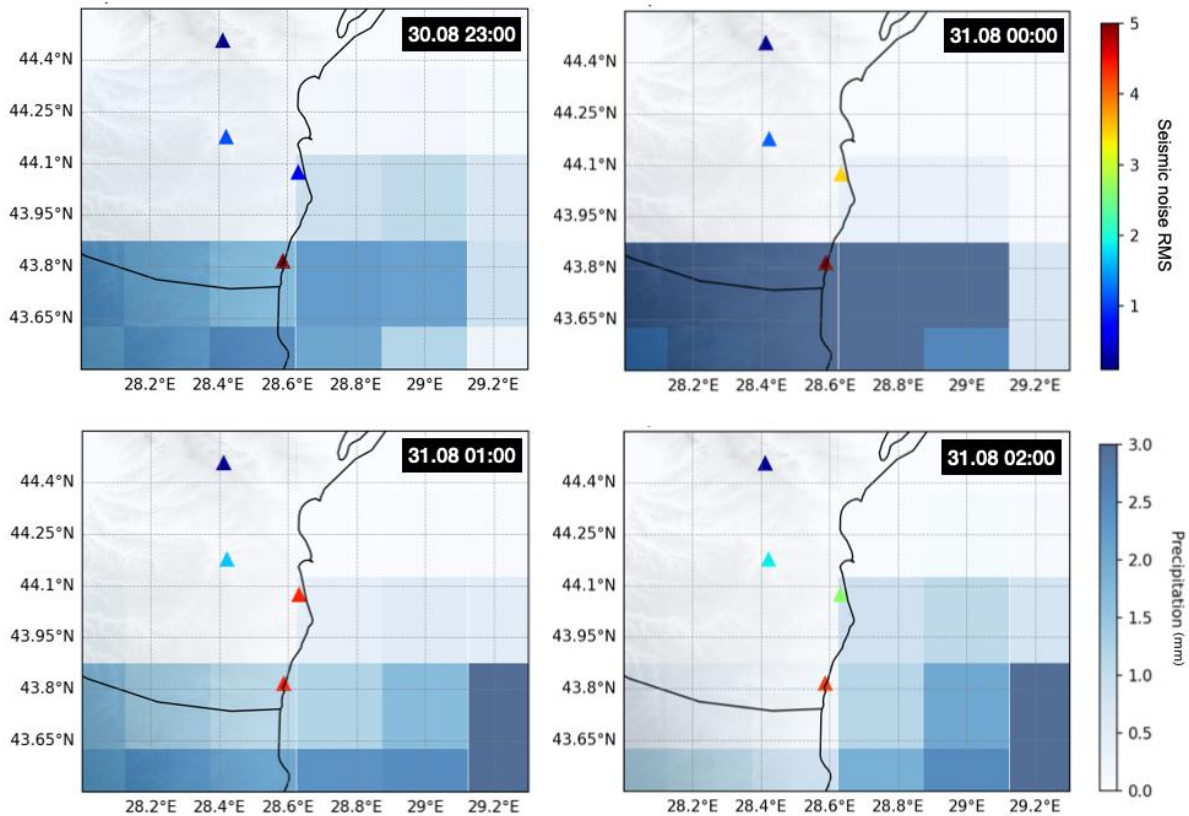


376

377 *Figure 4. High frequency (30-50Hz) observations of the storm at station MANR. a. Time series of total*  
378 *precipitation every 10 minutes from the ANM station at Mangalia b. Spectrogram of the seismic time series*  
379 *for station MANR. c. Envelope of the displacement seismogram at station MANR.*

380 To visualise the signature of the storm passing over the network of broadband seismic stations in  
381 the coastal area, we also plotted the hourly precipitation values with the hourly root-mean-square  
382 amplitudes of the high-frequency (>30 Hz) seismic velocity envelopes recorded at seismic stations.  
383 Figure 5 shows four snapshots of hourly plots of gridded precipitation data from ERA5, which  
384 have a lower amplitude than point measurements at the Mangalia station, due to the averaging over

385 the grid block. This figure presents a temporal coincidence between changing precipitation patterns  
 386 from ERA5 data and the amplitudes of high-frequency seismic noise. This observation further  
 387 supports the likelihood of a causal relationship. These high-frequency seismic signals could  
 388 potentially be explored as a near real time indicator of intense rainfall events, providing a  
 389 conceptual basis for a simple streaming detection approach.



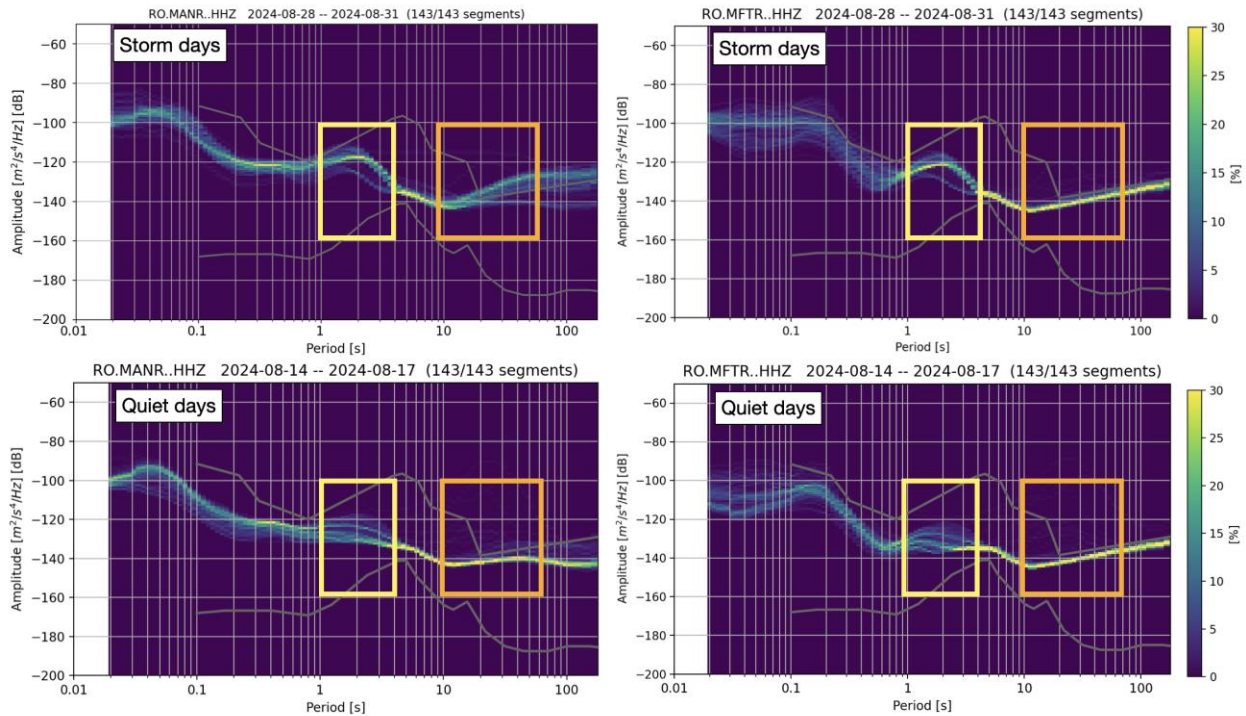
390  
 391 *Figure 5. Distribution of hourly RMS of high pass filtered (>30 Hz) seismograms and precipitation data.*  
 392 *Colours indicate hourly RMS amplitude of velocity envelopes filtered 30-50 Hz. Background coloured*  
 393 *grid indicates the total precipitation (mm) from ERA5 data.*

394 The analysis of the microseismic noise frequency band is closely linked to the interaction between  
 395 ocean waves and the seafloor, which is influenced by storm conditions. To assess the storm's  
 396 impact, we analyze the PPSD (Probabilistic Power Spectral Density) of noise recorded at several  
 397 stations during both storm and quiet days, using the latter as a baseline. Figure 6 shows examples  
 398 of PPSD at stations MANR and MFTR (Figure 2), revealing differences in PSD amplitudes across  
 399 the primary and secondary microseismic bands. These differences indicate the presence of high-  
 400 intensity wind-driven waves and swell energy in the sea.

401 The secondary microseismic band, in particular, shows a significant rise in amplitude during  
 402 storms, consistent with established mechanisms linking storm-driven wave activity and seafloor  
 403 pressure fluctuations (Figure 3) to enhanced secondary microseism generation, while local factors  
 404 such as bathymetry or wave direction may modulate the response (Bromirski et al., 2002; Ebeling

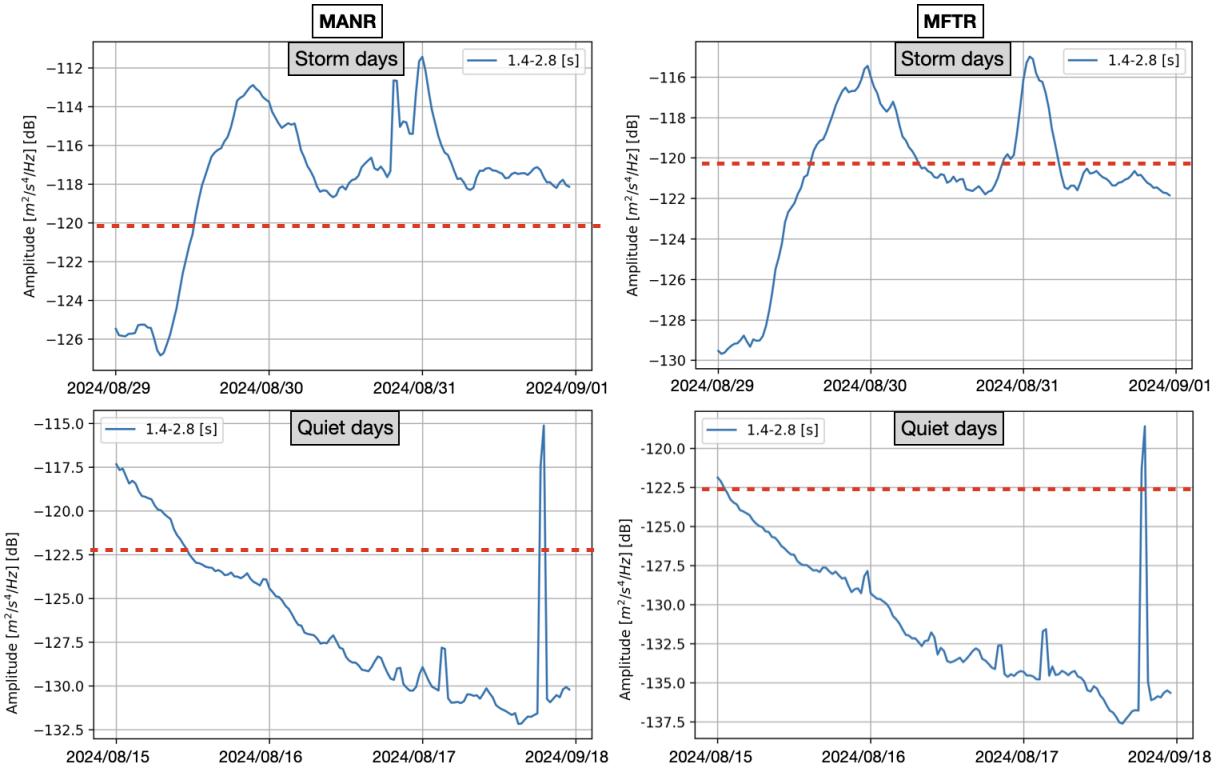
405 et al., 2012; Arduin et al., 2019). On quiet days, the PSD remains consistently lower, typically  
 406 staying below the -120 dB threshold. This stark contrast emphasizes the role of atmospheric  
 407 conditions in modulating seismic noise, with storms causing a notable increase in energy across  
 408 both frequency bands. The temporal evolution of the PSD values (Figure 7) further highlights the  
 409 storm's impact, with fluctuations corresponding to changes in environmental factors, reinforcing  
 410 the connection between storm activity and the observed seismic signals.

411



412  
 413 *Figure 6. Probabilistic Power Spectral Density (PPSD) plots for two seismic stations near the Black Sea*  
 414 *coast capturing the target storm signal in the microseismic bandwidths (marked with rectangles). The top*  
 415 *panels show the PPSD distributions across frequencies, indicating the probability of power spectral*  
 416 *density values in percentage for days including the Black Sea storm. The bottom panels show PPSD for*  
 417 *days with no recorded events.*

418 Anthropogenic seismic noise does not significantly affect the microseismic band (0.1-1 Hz).  
 419 Human-generated vibrations predominantly occupy frequencies above 1 Hz, while long-period  
 420 microseisms are produced by ocean wave interactions and are coherent over large distances. The  
 421 temporal evolution of the microseismic energy observed in this study matches changes in wave  
 422 state associated with the storm rather than any local activity. Similar to the findings of Gross &  
 423 Ritter (2009), the sub-Hz frequency range is dominated by natural sources, with anthropogenic  
 424 contributions being negligible.



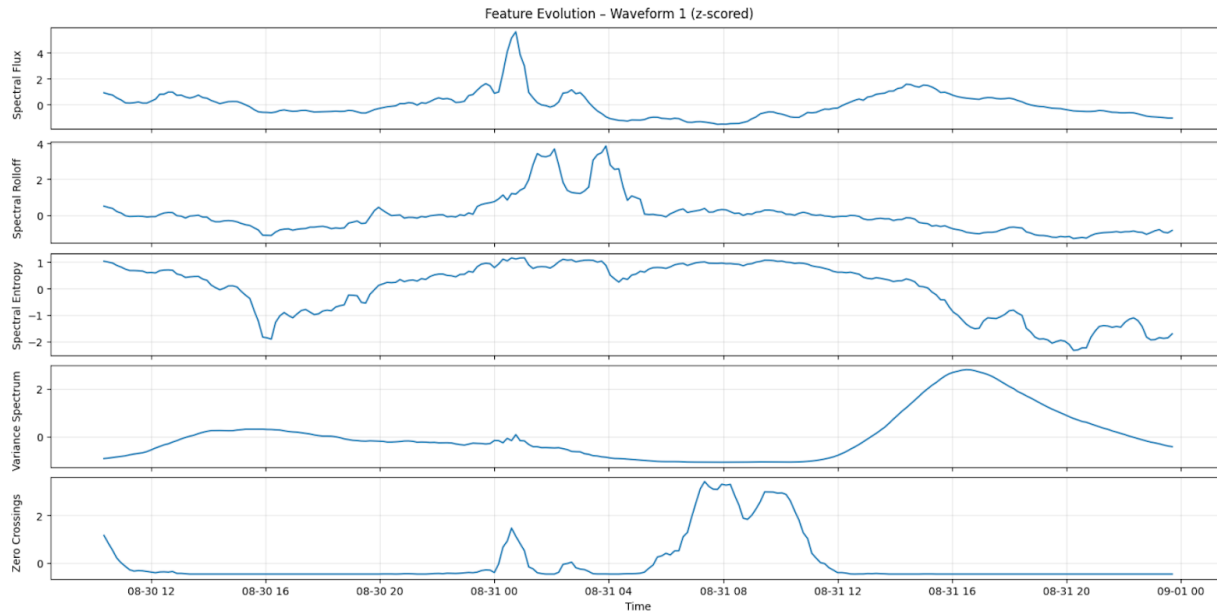
425

426 *Figure 7. Temporal PSDs for two seismic stations near the Black Sea Coast in the secondary microseismic*  
 427 *band showing significantly higher values ( $>-120$  dB) during stormy days compared to days without*  
 428 *recorded precipitation.*

## 429 4.2 Infrasonic and satellite lightning observations

### 430 4.2.1 Single-station feature extraction

431 The evolution of time-frequency features over the duration of the Black Sea storm revealed distinct  
 432 patterns in the infrasonic signal (Figures 8 and 9). Centroid and rolloff show parallel behavior  
 433 because they are both frequency-domain descriptors tied to the distribution of spectral energy, and  
 434 so both respond strongly to the same uplift in energy during the storm's peak. Spectral flux, by  
 435 contrast, quantifies inter-frame spectral change, so its peak occurs where the spectrum transitions  
 436 most rapidly, even when that does not coincide with the maximum absolute energy (e.g. Pásztor  
 437 et al., 2023). Finally, the zero-crossing rate reflects time-domain volatility, not spectral shape,  
 438 which explains its distinct pattern, such as the storm's later stages may introduce broadband  
 439 turbulence or noise components that boost zero crossings independently of the spectral shifts  
 440 visible in the first two panels. While the individual features varied over time, it is the combination  
 441 of these features through K-means clustering that effectively identifies the time frame  
 442 corresponding to the main precipitation episode. Zero-crossings exhibited more variable patterns,  
 443 reflecting high-frequency fluctuations, but the joint clustering of all features robustly captures the  
 444 timing of the storm's most intense phases.

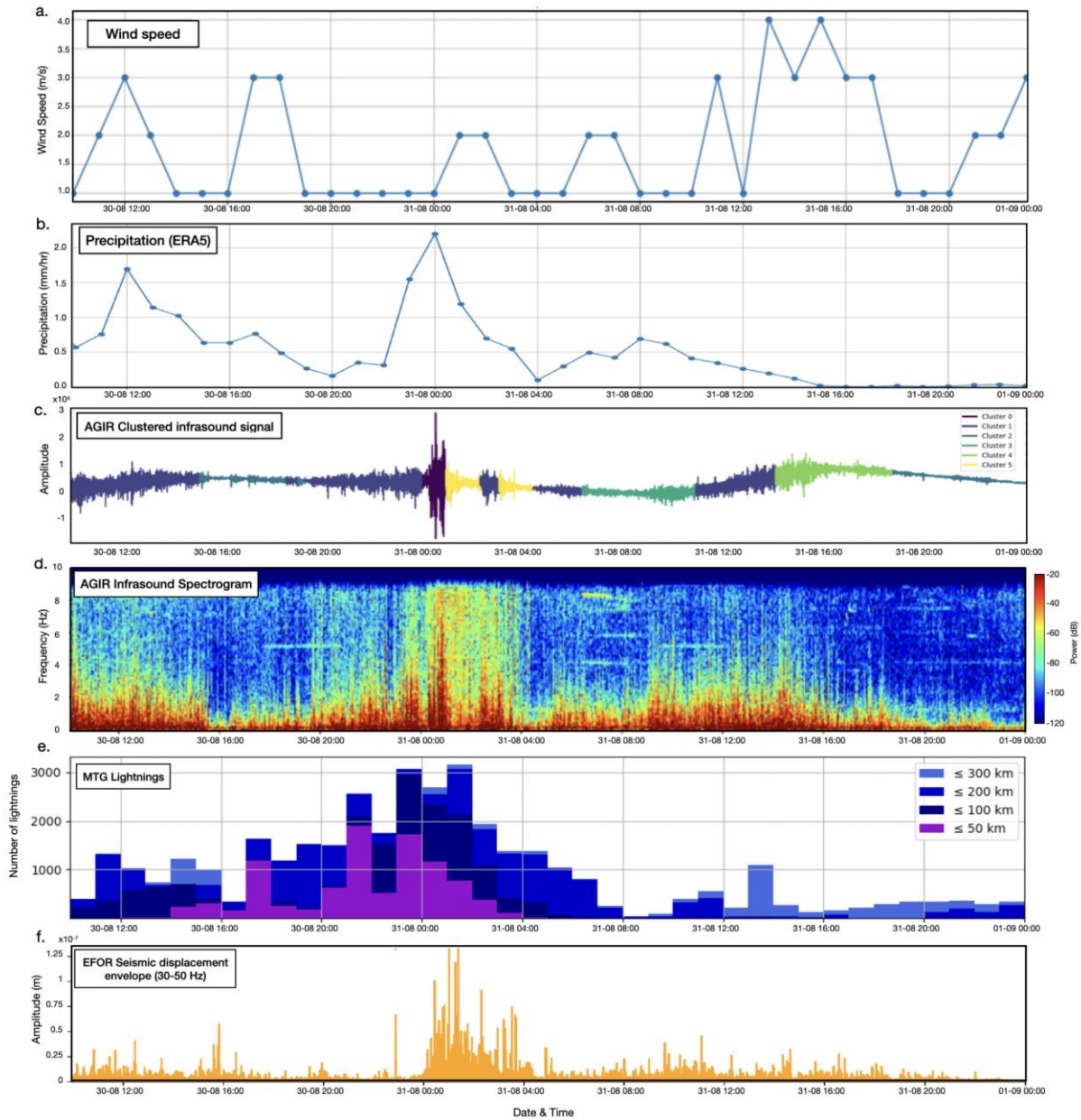


445

446 *Figure 8. Time-frequency feature analysis for the single-station infrasound signal recorded at AGIR during*  
 447 *the Black Sea Storm.*

448 K-means clustering separated the acoustic data into six groups with distinct spectral and amplitude  
 449 characteristics (Figure 9). These clusters highlight acoustic states that may relate to different  
 450 environmental conditions during the monitoring period. For example, Cluster 0 coincides with  
 451 periods of intense precipitation and stronger winds, and also aligns with enhanced lightning  
 452 activity, suggesting a link with the most energetic phases of the convective system. Cluster 1  
 453 captures intervals with moderate amplitudes but persistently elevated background acoustic levels,  
 454 without corresponding rainfall or wind peaks, and with comparatively reduced lightning  
 455 occurrence. Cluster 2 reflects calmer conditions with low amplitudes and little or no precipitation  
 456 and minimal lightning activity. Transitional patterns also arise, such as Cluster 3, which appear  
 457 before intervals grouped in Cluster 1 and mark intermediate acoustic activity. Overall, the  
 458 clustering approach demonstrates that combining multiple features reveals consistent acoustic  
 459 regimes and can help differentiate environmental conditions, without relying on any single  
 460 parameter.

461 Interestingly, the spectral content of the infrasound signal showed similarities to seismic signal  
 462 envelopes, particularly in the high frequency ranges (Figure 9), which may suggest a connection  
 463 between the atmospheric pressure waves detected by infrasound and the ground vibrations  
 464 captured by seismic instruments. When considered alongside the temporal evolution of lightning  
 465 activity, this overlap implies that both seismic and infrasound signals could be complementary in  
 466 capturing different aspects of storm dynamics, with seismic signals reflecting ground vibrations  
 467 and infrasound capturing the atmospheric processes, and lightning indicating convective intensity.



468  
 469 *Figure 9. Clustering results of infrasound signals recorded at AGIR from the August Black Sea storm event*  
 470 *compared with precipitation data and seismic signal from EFOR station. a. Wind speed per hour measured*  
 471 *at ANM meteorological station Constanta; b. Average precipitation data from  $1^{\circ} \times 1^{\circ}$  around AGIR. c. Raw*  
 472 *infrasound signal recorded at the AGIR sensor during the period of August 30–31, 2024, with different*  
 473 *segments color-coded according to the cluster they belong to, based on K-means clustering of 30-minute*  
 474 *time-frequency feature windows. d. The corresponding spectrogram generated using Blackman windowing*  
 475 *with 128 samples and 70% overlap; e. Number of lightnings detected by the MTG satellite. f. Seismic*  
 476 *displacement envelope at station EFOR, filtered between 30–50 Hz.*

477

478

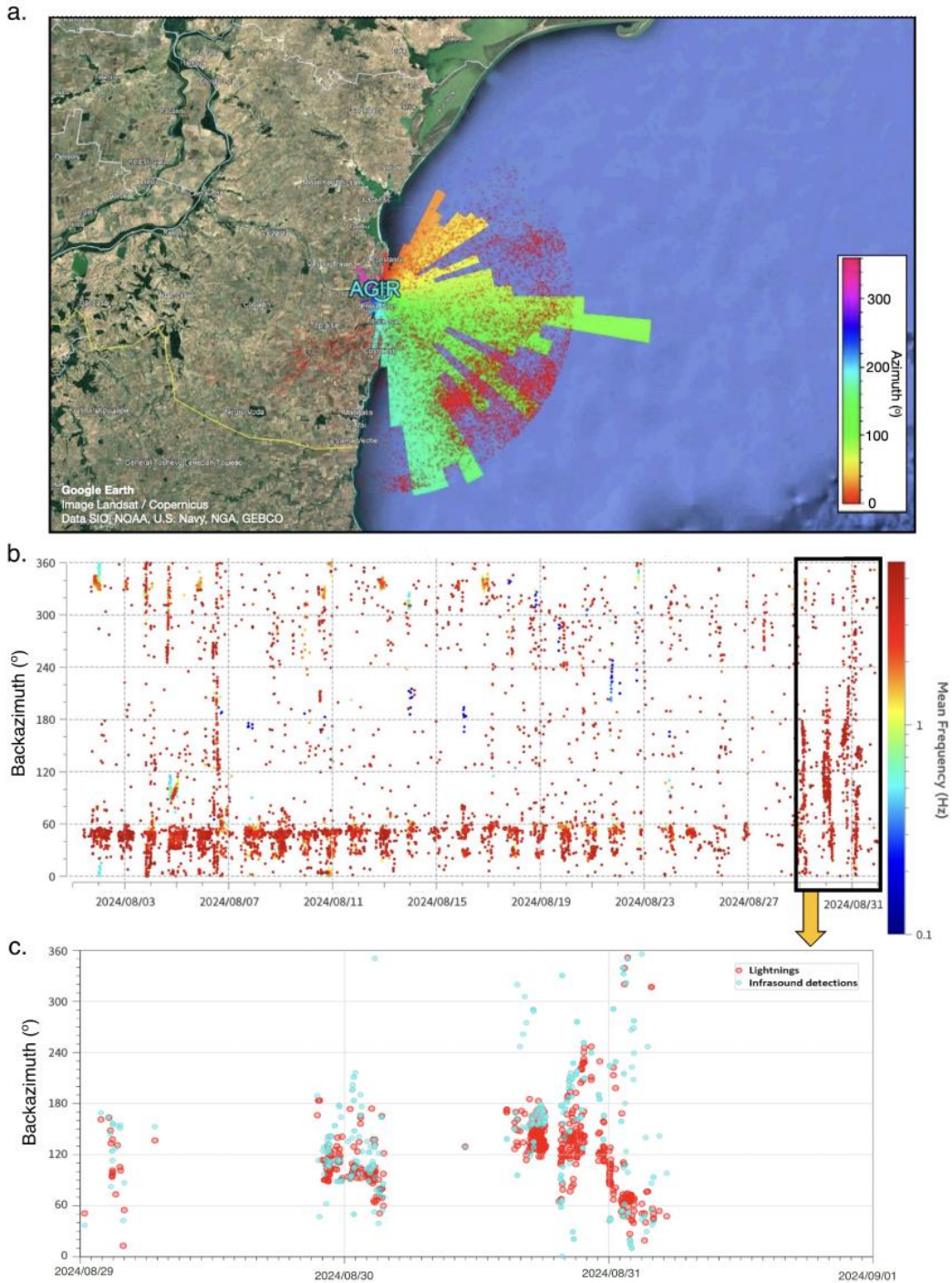
479

#### 480 4.2.2 Array analysis and lightning detection

481 Using multiple sensors from the AGIR infrasound array with the PMCC algorithm allowed us to  
482 isolate coherent infrasound signals and estimate their propagation parameters, such as backazimuth  
483 and arrival times, across the sensor network. Nearly 11,000 lightning flashes were detected by the  
484 MTG Lightning Imager within 50 km of the AGIR station during the Black Sea storm (Figure  
485 10a), providing a dense reference set for comparison. Within the relevant 0.6-7 Hz frequency band,  
486 approximately 1,100 infrasound detections were identified. These signals primarily consisted of  
487 long-duration wave trains with frequent amplitude peaks and short-lived disturbances  
488 characteristic of lightning-generated infrasound. Their dominant frequency was around 3 Hz, and  
489 amplitudes ranged from 0.01 to 3.4 Pa (Figure 10b).

490 A subset of the infrasound detections could be confidently associated with individual lightning  
491 discharges based on temporal alignment and backazimuth consistency. Overall, we were able to  
492 associate 6.4% of lightning flashes with infrasound detections at AGIR (Figure 10c). This level of  
493 correspondence is reasonable given that only a subset of lightning discharges radiate infrasound  
494 efficiently and that propagation strongly depends on altitude, source geometry, and atmospheric  
495 conditions. Nevertheless, these coincident detections demonstrate that lightning-generated  
496 infrasound was clearly recorded during the storm and that the PMCC-derived acoustic signatures  
497 provide valuable insight into the evolution of electrical activity and storm dynamics.

498 Anthropogenic noise sources, such as wind turbines (e.g., Jakobsen, 2005), industrial machinery  
499 (Gastmeier and Howe, 2008), and road traffic (Grafkina et al., 2019), are well-documented  
500 challenges for infrasound studies because they often generate persistent, periodic, or tonal signals  
501 that can mask natural atmospheric phenomena. The AGIR infrasound array used here is located in  
502 a semi-rural setting, distant from major roads and industrial facilities, which reduces the likelihood  
503 of local anthropogenic contamination. Several independent lines of evidence indicate that such  
504 contamination is negligible in this case study. First, the strongest infrasound signatures occurred  
505 during night-time hours, when human activity is minimal. Second, both the clustering and PMCC  
506 analyses identify transient signals with energy peaking around  $\sim 3$  Hz, which contrasts sharply with  
507 the more continuous or harmonic spectral patterns typically produced by anthropogenic sources.  
508 Third, the temporal alignment of these acoustic signatures with independent observations of  
509 lightning and precipitation provides strong confirmation that the detected infrasound variability is  
510 storm-related rather than anthropogenic in origin.



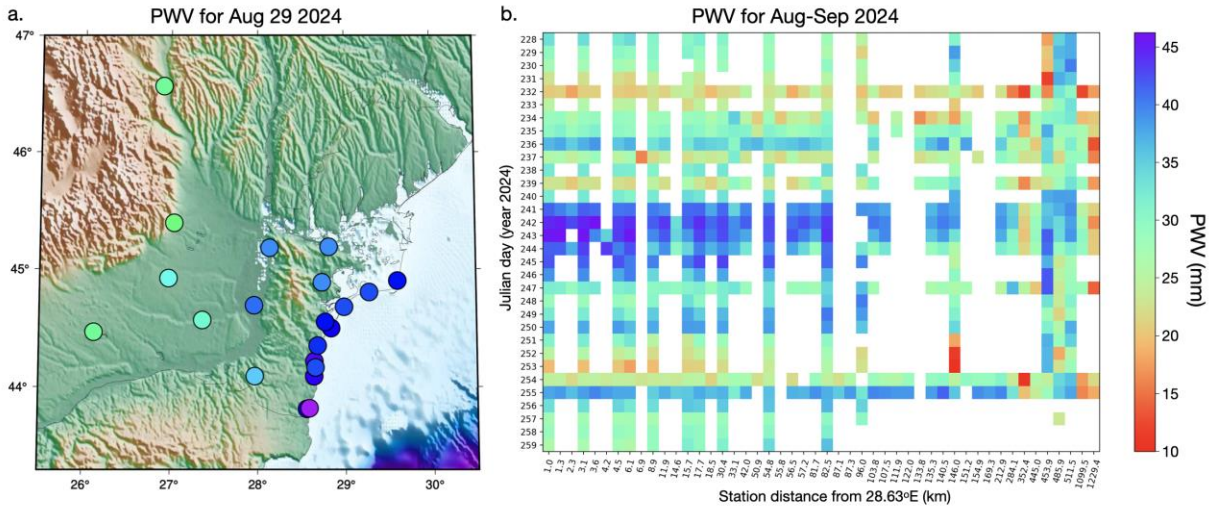
511

512 *Figure 10. a. Polar histogram of infrasound detections from the AGIR station, displayed with © Google*  
 513 *Earth, along with the locations of lightning strikes detected by the MTG Lightning Imager system for the*  
 514 *period from 29-31st of August 2024. The geographical position of the AGIR infrasound station is also*  
 515 *shown on the map. b. diagram of high-frequency detections from the AGIR infrasound station between 1-*  
 516 *31st of August 2024. c. Associations between events detected by the AGIR infrasound array and the MTG*  
 517 *satellite database for 29-31st of August 2024.*

518 **4.3 GNSS-derived precipitable water vapor trends**

519 The analysis of daily GNSS-derived precipitable water vapor (Figure 11) reveals clear temporal  
520 variations, with the highest PWV values consistently recorded on stormy days (>40 mm on DOY  
521 240-243, i.e. August 27-30). Notably, the peak values occurred between DOY 241 and DOY 243  
522 (Figure 11b), when the heaviest rainfall was observed (Figure 1). Coastal stations showed  
523 extremely high PWV values (>40 mm) compared to inland stations (<30 mm), with a slight  
524 decrease in PWV away from the coast (Figure 11a). This spatial distribution highlights the  
525 geographical gradient of atmospheric moisture, with the highest PWV concentrations near coastal  
526 areas, also decreasing gradually toward the north away from the storm peak. Interestingly, some  
527 inland stations (BUCU, PGNL, RMSR) recorded their peak PWV on DOY 255, corresponding to  
528 the onset of the Boris storm, another significant extreme rainfall event that swept through Central  
529 and Eastern Europe (Athanasé et al., 2024).

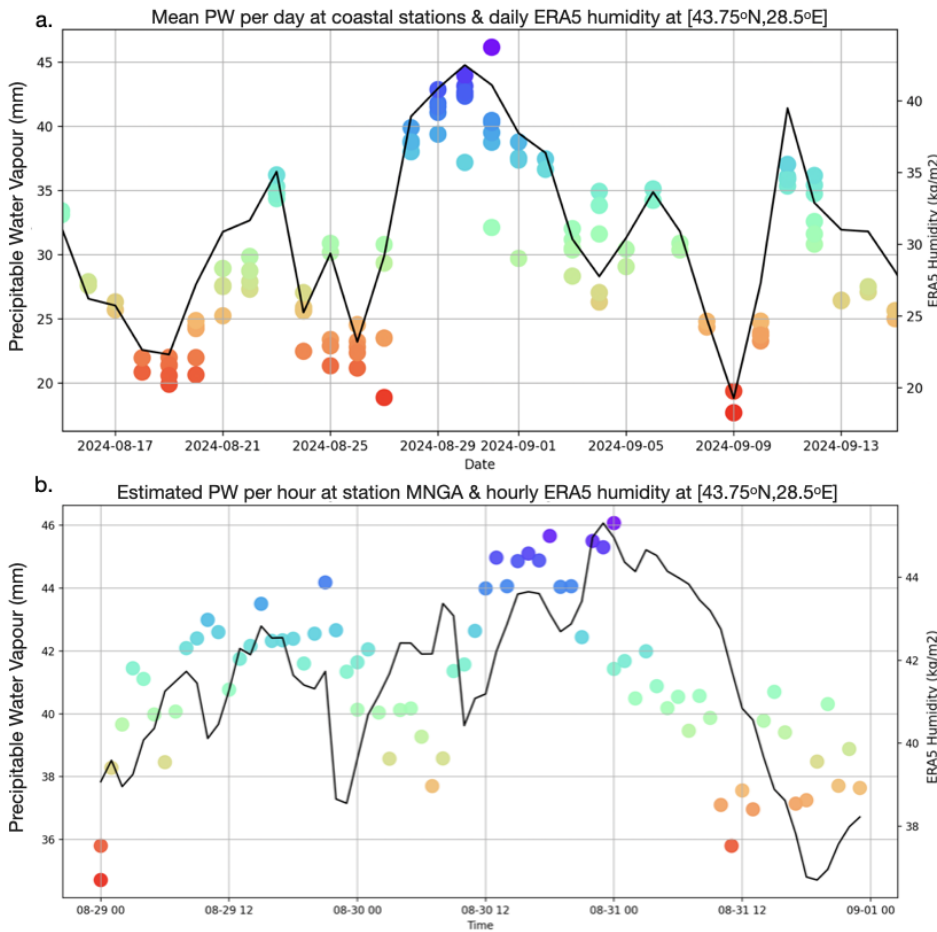
530 Elevated PWV was observed as early as August 27th (Figure 12a), suggesting that the tropospheric  
531 moisture loading began to increase several days before the onset of the rainfall. This increase in  
532 PWV may act as an indicator of a developing weather system. Remarkably, although HAR1,  
533 located inland, did not directly experience the extreme rainfall, it exhibited similar PWV behavior  
534 to coastal stations, suggesting that GNSS stations, even outside the immediate storm zones, can  
535 capture atmospheric signals indicative of intense precipitation. This finding offers a valuable  
536 precedent, showing that PWV measurements at GNSS stations not directly in the storm path can  
537 still provide critical insights into moisture dynamics at the tropospheric level. The comparison  
538 with ERA5’s total-column water vapour further supports this interpretation, as the broad temporal  
539 evolution of ERA5 humidity mirrors the GNSS-derived daily PWV patterns, despite the inherently  
540 coarser resolution of the reanalysis data.



541  
542 *Figure 11. a: Map of GNSS stations coloured as a function of PWV estimated for the 29th of August. b.*  
543 *Daily PWV values for each station, plotted as a function of their longitudinal distance relative to 28.63°E.*

544 Using the hourly PWV data, Figure 12b illustrates the evolution of water vapour at the MNGA  
545 station, which recorded the heaviest rainfall in the study area. Notably, MNGA also showed a rapid

546 buildup of PWV, reaching values greater than 44 mm just a few hours before the storm event. This  
 547 rapid increase in PWV suggests that the accumulation of atmospheric moisture may precede to  
 548 extreme weather events, such as intense rainfall and storms. This observation aligns with known  
 549 atmospheric dynamics, where a significant increase in water vapor content precedes heavy  
 550 precipitation, highlighting the potential usefulness of GNSS-based PWV monitoring for studying  
 551 pre-storm atmospheric moisture variability. The general rising trend toward the event is present in  
 552 both GNSS-based and ERA5 reanalysis datasets, although some minor fluctuations are not  
 553 matched. After the storm, the GNSS PWV drops sharply while ERA5 maintains elevated values  
 554 for several hours. These differences show that GNSS can resolve rapid, real-time atmospheric  
 555 changes that may be blurred in large-scale weather model products.



556

557 *Figure 12. Comparison of GNSS-derived precipitable water vapor (coloured circles) with independent*  
 558 *humidity data (black line) from ERA5's total column vertically integrated water vapor parameter. a. Mean*  
 559 *PWV values per day at selected GNSS stations (CONB, HARI, MNGA, MNGL, MNGM, TUZL) alongside*  
 560 *daily averaged ERA5 humidity. b. Estimated PWV values per hour at the MNGA GNSS station compared*  
 561 *with hourly ERA5 humidity at the 43.75°N, 28.5°E grid point. In both panels, GNSS data points are*  
 562 *represented by colored circles where the color scale corresponds to the PWV magnitude, consistent with*  
 563 *the vertical axis.*

564

## 565 5. Discussion

566 Storm evolution, in the meteorological sense, describes the sequence of processes from pre-storm  
567 atmospheric moisture accumulation to convective initiation, peak rainfall, electrical activity, and  
568 the associated marine response along coastal areas. The multi-sensor dataset used here captures  
569 these different stages: GNSS-PWV documents the build-up of column water vapor before  
570 convective onset, infrasound detects lightning-generated acoustic waves and pressure disturbances  
571 during the mature convective phase, high-frequency seismic noise reflects the timing and spatial  
572 progression of intense rainfall at the surface, microseisms respond to storm-driven changes in sea  
573 state, and ERA5/MTG provide the mesoscale structure that ties these geophysical signals together.  
574 By observing the same storm through these complementary physical pathways, we can outline a  
575 more detailed picture of how the storm developed, intensified, and decayed than is possible from  
576 individual datasets.

577 The integration of infrasound, seismic, and GNSS data in monitoring the extreme storm event over  
578 the Black Sea provides valuable insights into the dynamics of storm behavior and illustrates the  
579 potential of repurposing non-conventional sensors for meteorological analysis. Infrasound data,  
580 for instance, revealed a clear acoustic signature of lightning activity, with signals detected in the  
581 range of 0.6 to 7 Hz corresponding to electrical discharges. The high frequency of infrasound  
582 detections (around 1,100) suggests that it may provide useful information for tracking storm-  
583 related phenomena, particularly lightning, which is difficult to capture with traditional methods.  
584 However, the signals did not always perfectly align with lightning strikes, indicating that other  
585 factors, such as the movement of storm systems or variations in atmospheric conditions, may  
586 influence infrasound signatures. This suggests that refining the correlation between infrasound  
587 signals and lightning activity could be an avenue for future research, particularly in cases of sparse  
588 lightning or in remote regions.

589 Seismic data alone also showed a strong connection between high-frequency seismic noise and  
590 heavy rainfall, supporting previous studies that linked seismic signals to rainfall intensity. The  
591 distinction between high-frequency and low-frequency seismic noise is particularly noteworthy.  
592 Increases in high-frequency seismic noise occurred during intense precipitation, while low-  
593 frequency signals were associated with wave height and storm-driven winds. This suggests that  
594 different seismic frequencies capture distinct storm dynamics, with high-frequency signals  
595 reflecting localized rainfall impacts and low-frequency signals tied to broader atmospheric and  
596 oceanic interactions. This dual-frequency approach provides a more nuanced interpretation of  
597 seismic data in storm monitoring, highlighting its complexity.

598 A key finding of this study is that K-means clustering of multiple acoustic features, including  
599 spectral centroids, roll-off, flux, and zero-crossing rate, effectively segmented the infrasound  
600 record into distinct storm phases. This approach proved more robust than relying on any single  
601 feature, as the combination captured the complex, evolving nature of the storm's acoustic signature.  
602 For instance, the identified clusters delineated periods of intense precipitation, elevated  
603 background acoustic levels, and calm intervals, providing a data-driven overview of the storm's  
604 progression. The fact that these acoustically defined phases align with independent meteorological  
605 observations, such as rainfall peaks, confirms that the infrasound signal variability is a direct  
606 response to the storm's atmospheric dynamics.

607 Furthermore, the observed spectral similarity between the infrasound signals and high-frequency  
608 seismic envelopes suggests a coupled seismo-acoustic response to the storm. This implies that the  
609 same atmospheric forcing, such as pressure fluctuations from rainfall and wind, generates  
610 complementary signals in the atmosphere (infrasound) and the ground (seismic waves). Our  
611 findings are consistent with other studies of intense weather systems, where coupled microbarom-  
612 microseism signals have been shown to track storm structure and evolution (e.g., Butler & Aucan,  
613 2018; Smirnov, 2021). The coherent acoustic and seismic responses to atmospheric-oceanic  
614 pressures, as also documented in Distributed Acoustic Sensing studies (Taweessintananon et al.,  
615 2023) and surf studies (Francoeur et al., 2025), reinforce the interpretation of a shared source  
616 mechanism. Therefore, a major and logical next step is to move beyond analyzing these datasets  
617 in parallel and to perform joint clustering of seismo-acoustic data (e.g. Floroiu et al., 2025). Such  
618 an integrated approach could unlock a more comprehensive, multi-physics understanding of storm  
619 dynamics by simultaneously characterizing the coupled atmospheric and ground-borne wavefields.

620 The temporal variations observed in GNSS-derived integrated precipitable water vapor provide  
621 valuable insights into atmospheric moisture dynamics before extreme weather events. The  
622 pronounced increase in PWV, particularly in the days leading up to and during the storm, supports  
623 the link between elevated atmospheric water vapor and precipitation. Notably, the PWV buildup  
624 starting roughly three days before the extreme rainfall suggests that rising moisture levels in the  
625 troposphere were observed prior to the intense precipitation in this event. Even stations located up  
626 to 130 km inland, such as HAR1, recorded similar PWV trends, indicating that GNSS stations  
627 outside direct storm zones can still provide crucial atmospheric data. Hourly PWV trends further  
628 revealed a rapid increase several hours before precipitation, with values exceeding 44 mm/hr,  
629 highlighting the accumulation of moisture just before heavy rainfall. These findings align with the  
630 notion that increasing atmospheric moisture acts as a precursor to intense precipitation,  
631 highlighting the potential of GNSS-based PWV monitoring for tracking moisture and  
632 understanding short-term atmospheric fluctuations.

633 The integration of GNSS, infrasound, and seismic data provides a more comprehensive  
634 understanding of storm dynamics than any single data source alone. The synergy between these  
635 diverse sensor types allows for the detection of atmospheric moisture, lightning activity, rainfall-  
636 induced seismic signals, and storm-driven oceanic interactions. Future research should focus on  
637 refining unsupervised learning algorithms for infrasound and seismic signal classification,  
638 optimizing joint clustering techniques, and improving the integration of these data sources to  
639 enhance storm forecasting and early-warning systems. This case study suggests that this multi-  
640 sensor approach may help improve our ability to predict extreme weather events, understand their  
641 impacts, and mitigate associated risks.

## 642 **6. Conclusions**

643 This study presents a comprehensive analysis of a record-breaking storm over the Black Sea, using  
644 a combination of GNSS, infrasound, and seismic data to capture the dynamics of extreme weather  
645 events. Our findings underscore the power of multi-sensor networks in enhancing the  
646 understanding of storm behavior, particularly in the context of atmospheric moisture, lightning  
647 activity, and storm-induced seismic signals. GNSS-derived integrated precipitable water vapor  
648 indicates a clear buildup of atmospheric moisture hours before the onset of heavy rainfall,  
649 providing valuable insights into the lead-up to extreme precipitation events. Infrasound and

650 seismic data further complemented this analysis, with infrasound providing useful observations of  
651 lightning activity and seismic data revealing the link between rainfall intensity and high-frequency  
652 seismic noise.

653 The storm analysed here represents an exceptional meteorological event and one of the most  
654 intense storms recorded in the region in recent years. An attribution analysis using the ClimaMeter  
655 framework (Antonescu et al., 2024) identified a detectable anthropogenic climate change signal  
656 associated with this event, placing it within the broader context of intensifying extremes in a  
657 warming climate. The integration of GNSS, infrasound, and seismic data provides a more nuanced  
658 and holistic view of storm dynamics, highlighting the need for advanced monitoring systems to  
659 predict and respond to such extreme events. Looking forward, such multi-sensor approaches may  
660 support future developments in integrated environmental monitoring and research into early-  
661 warning capabilities, ultimately contributing to improved understanding and characterization of  
662 high-impact atmospheric events.

## 663 **7. Code availability**

664 Seismic data were processed with the open-source python framework for seismology Obspy  
665 (Beyreuther et al., 2010). Infrasound data was processed with the WinPMCC software (Le Pichon  
666 et al., 2010) developed by CEA/DASE (French Atomic Energy Commission, Environmental  
667 Assessment and Monitoring Department) and open-source Python libraries for signal processing.  
668 Some of the figures were made with GMT (Generic Mapping Tools, Wessel et al., 2019). The  
669 GNSS data was processed using Gamit/Globk (Herring et al., 2020) developed by Massachusetts  
670 Institute of Technology (<http://www-gpsg.mit.edu/gg/>).

## 671 **8. Data availability**

672 Processed infrasound, seismic, and GNSS-derived integrated water vapour data can be visualized  
673 and accessed via the INFP monitoring platforms: <https://infp.ro/dashboard-reactive.php> and  
674 <https://reactive.infp.ro/events/>. Seismic data are part of the Romanian National Seismic Network  
675 maintained by the National institute for Earth Physics (NIEP, [www.infp.ro](http://www.infp.ro)) and are freely  
676 available in the miniseed format via EIDA (European Integrated Data Archive,  
677 <https://www.orfeus-eu.org/data/eida/>). GNSS data are available for download from NIEP  
678 (<http://gps.infp.ro/#/download>) and are provided in the standardized RINEX v2 format, with 24-  
679 hour files sampled at 30-second intervals. Infrasound data at AGIR are available to download from  
680 NIEP via FDSN dataselect web service. Hourly hydro-meteorological data were obtained from the  
681 Copernicus Climate Change Service, Climate Data Store (<https://doi.org/10.24381/cds.bd0915c6>),  
682 ERA5 dataset (Hersbach et al., 2023). Limited wind and precipitation data were downloaded from  
683 the National Meteorological Agency from <https://www.meteoromania.ro/grafice/> (accessed on  
684 13.09.2024) and from [https://www.meteoromania.ro/clim/caracterizare-lunara/cc\\_2024\\_08.html](https://www.meteoromania.ro/clim/caracterizare-lunara/cc_2024_08.html)  
685 (accessed on 10.11.2025), respectively. Lightning data came from Meteosat Third Generation  
686 Lightning Imager operated by EUMETSAT (The European Organisation for the Exploitation of  
687 Meteorological Satellites, <https://www.eumetsat.int/>).

688

## 689 **9. Author contribution**

690 **Laura Petrescu:** Conceptualization, Methodology, Software, Formal analysis, Data Curation,  
691 Writing-Original Draft, Visualization; **Bogdan Antonescu:** Conceptualization, Writing-Review &  
692 Editing, Visualization; **Sorin Nistor:** Software, Formal Analysis, Data curation, Visualisation,  
693 Writing-Review & Editing; **Iustin Floroiu:** Methodology, Software, Formal analysis, Data  
694 Curation, Writing-Original Draft, Visualization; **Dragoş Ene:** Software, Formal analysis, Data  
695 Curation, Writing-Review & Editing; **Daniela Ghica:** Software, Formal analysis, Data Curation;  
696 **Constantin Ionescu:** Funding Acquisition, Resources, Project administration; **Andrei Anghel:**  
697 Methodology, Supervision; **Mihai Dăţcu:** Methodology, Supervision, Funding Acquisition,  
698 Resources, Project administration.

## 699 **10. Acknowledgments**

700 We would like to thank the technicians and staff at NIEP for their support in installing,  
701 maintaining, and ensuring the proper functioning of the equipment used in this study. Additionally,  
702 we appreciate the efforts of those involved in data formatting and preparation (Cristian Neagoe,  
703 Eduard Nastase, Victorin Toader) which were essential for this work. We also thank the two  
704 anonymous reviewers for their valuable feedback, which helped improve the manuscript.

## 705 **11. Financial support**

706 This work was carried out in the framework of the “Competence Center for Climate Change Digital  
707 Twin for Earth forecasts and societal redressment” Project PNRR- DTEClimate nr.  
708 760008/31.12.2023, subproject Reactive “The Research center for climate change due to natural  
709 disasters and extreme weather events”, supported by the Ministry of Research, Innovation and  
710 Digitalization of Romania.

## 711 **12. References**

712 Antonescu, B., Dafis, S., & Faranda, D.: Changes in precipitation patterns driving August 2024  
713 Romania floods mostly driven by human-driven climate change. *ClimaMeter, Institut Pierre*  
714 *Simon Laplace, CNRS*. <https://doi.org/10.5281/zenodo.14056214>, 2018.

715 Ardhuin, F., Gualtieri, L., Stutzmann, E., Nakata, N. and Fichtner, A.: Physics of ambient noise  
716 generation by ocean waves. In *Seismic ambient noise*, Eds: Nakata, N., Gualtieri, L., Fichtner, A.  
717 Cambridge University Press, 69-108, <https://doi.org/10.1017/9781108264808.005>, 2019.

718 Assink, J. D., Evers, L. G., Holleman, I., and Paulssen, H.: Characterization of infrasound from  
719 lightning, *Geophysical Research Letters*, 35, L15802, <https://doi.org/10.1029/2008GL034193>,  
720 2008.

721 Aster, R.C., McNamara, D.E. & Bromirski, P.D.: Multidecadal climate-induced variability in  
722 microseisms. *Seismological Research Letters*, 79(2), 194-202,  
723 <https://doi.org/10.1785/gssrl.79.2.194>, 2008.

- 724 Aster, R.C., Ringler, A.T., Anthony, R.E., & Lee, T.A.: Increasing ocean wave energy observed  
725 in Earth's seismic wavefield since the late 20th century. *Nature Communications*, 14(1), 6984,  
726 <https://doi.org/10.1038/s41467-023-42673-w>, 2023.
- 727 Athanase, M., Sánchez-Benítez, A., Monfort, E., Jung, T. and Goessling, H.F.: How climate  
728 change intensified storm Boris' extreme rainfall, revealed by near-real-time storylines.  
729 *Communications Earth & Environment*, 5(1), 676, <https://doi.org/10.1038/s43247-024-01847-0>,  
730 2024.
- 731 Awange, J.L.: Environmental monitoring using GNSS: Global navigation satellite systems,  
732 Springer, Heidelberg, <https://doi.org/10.1007/978-3-540-88256-5>, 2012.
- 733 Beyreuther, M., Barsch, R., Krischer, L., Megies, T., Behr, Y. and Wassermann, J.: ObsPy: A  
734 Python toolbox for seismology. *Seismological Research Letters*, 81(3), 530-533,  
735 <https://doi.org/10.1785/gssrl.81.3.530>, 2010.
- 736 Bengtsson, L., Hodges, K.I. and Roeckner, E.: Storm tracks and climate change. *Journal of*  
737 *climate*, 19(15), 3518-3543, <https://doi.org/10.1175/JCLI3815.1>, 2006.
- 738 Bližňák, V. and Sokol, Z.: First validation of the Lightning Imager aboard Meteosat Third  
739 Generation satellite with Earth Networks Total Lightning Network. *International Journal of*  
740 *Applied Earth Observation and Geoinformation*, 147, 105205,  
741 <https://doi.org/10.1016/j.jag.2026.105205>, 2026.
- 742 Bollinger, L., Perrier, F., Avouac, J.P., Sapkota, S., Gautam, U., Tiwari, D.R.: Seasonal  
743 modulation of seismicity in the Himalaya of Nepal, *Geophysical Research Letters*, 34(8),  
744 <https://doi.org/10.1029/2006GL029192>, 2007.
- 745 Bondár, I., Šindelářová, T., Ghica, D., Mitterbauer, U., Liashchuk, A., Baše, J., Chum, J., Czanik,  
746 C., Ionescu, C., Neagoe, C. and Pásztor, M.: Central and Eastern European Infrasound Network:  
747 contribution to infrasound monitoring, *Geophysical Journal International*, 230(1), 565-579,  
748 <https://doi.org/10.1093/gji/ggac066>, 2022.
- 749 Borzì, A.M., Minio, V., Cannavò, F., Cavallaro, A., D'Amico, S., Gauci, A., De Plaen, R., Lecocq,  
750 T., Nardone, G., Orasi, A., Picone, M., Cannata, A.: Monitoring extreme meteo-marine events in  
751 the Mediterranean area using the microseism (Medicane Apollo case study). *Scientific Reports*,  
752 12(1), <https://doi.org/10.1038/s41598-022-25395-9>, 2022.
- 753 Bosy, J., Kaplon, J., Rohm, W., Sierny, J. and Hadas, T.: Near real-time estimation of water vapour  
754 in the troposphere using ground GNSS and the meteorological data, *Annales Geophysicae*, 30,  
755 1379–1391, <https://doi.org/10.5194/angeo-30-1379-2012>, 2012.
- 756 Brachet, N., Brown, D., Le Bras, R., Cansi, Y., Mialle, P., Coyne, J.: Monitoring the Earth's  
757 Atmosphere with the Global IMS Infrasound Network, in: *Infrasound Monitoring for Atmospheric*

- 758 Studies, edited by: Le Pichon, A., Blanc, E., Hauchecorne, A. , Springer, Dordrecht,  
759 [https://doi.org/10.1007/978-1-4020-9508-5\\_3](https://doi.org/10.1007/978-1-4020-9508-5_3), 2010.
- 760 Bromirski, P.D. and Duennebier, F.K.: The near-coastal microseism spectrum: Spatial and  
761 temporal wave climate relationships. *Journal of Geophysical Research: Solid Earth*, 107(B8), ESE  
762 5-1-ESE 5-20, <https://doi.org/10.1029/2001JB000265>, 2002.
- 763 Bruyninx, C., Habrich, H., Söhne, W., Kenyeres, A., Stangl, G. and Völksen, C.: Enhancement of  
764 the EUREF permanent network services and products, in: Proceedings of the International  
765 Association of Geodesy, *Symposium on Geodesy for Planet Earth, Buenos Aires, Argentina, 31*  
766 *August-4 September 2009*, 27-34, 2012.
- 767 Burtin, A., Hovius, N. and Turowski, J.M.: Seismic monitoring of torrential and fluvial processes.  
768 *Earth Surface Dynamics*, 4(2), 285-307, <https://doi.org/10.5194/esurf-4-285-2016>, 2016.
- 769 Butler, R. and Aucan, J.: Multisensor, microseismic observations of a hurricane transit near the  
770 ALOHA cabled observatory. *Journal of Geophysical Research: Solid Earth*, 123(4), 3027-3046,  
771 2018.
- 772 Campus, P. and Christie, D.R.: Worldwide observations of infrasonic waves, in: Infrasond  
773 monitoring for atmospheric studies, edited by: Le Pichon, A., Blanc, E., Hauchecorne, A.,  
774 Springer, Dordrecht, Netherlands, 185-234, [https://doi.org/10.1007/978-1-4020-9508-5\\_6](https://doi.org/10.1007/978-1-4020-9508-5_6), 2009.
- 775 Cansi, Y. and Pichon, A.L.: Infrasond event detection using the progressive multi-channel  
776 correlation algorithm, in: *Handbook of signal processing in acoustics.*, edited by: Havelock, D.,  
777 Kuwano, S., Vorländer, M., Springer, New York, 1425-1435, [https://doi.org/10.1007/978-0-387-30441-0\\_77](https://doi.org/10.1007/978-0-387-30441-0_77), 2008.
- 779 Coates, A. and Ng, A.Y.: Learning feature representations with k-means. In *Neural Networks:  
780 Tricks of the Trade: Second Edition (561-580)*. Berlin, Heidelberg: Springer Berlin Heidelberg,  
781 2012.
- 782 Coviello, V., Palo, M., Adirosi, E. and Picozzi, M.: Seismic signature of an extreme hydro-  
783 meteorological event in Italy, *Natural Hazards*, 1(1), 17, <https://doi.org/10.1038/s44304-024-00018-7>, 2024.
- 785 Diaz, J., Ruiz, M., Udina, M., Polls, F., Martí, D., Bech, J.: Monitoring storm evolution using a  
786 high-density seismic network, *Scientific Reports*, 13(1), <https://doi.org/10.1038/s41598-023-28902-8>, 2023.
- 788 Díaz, J., Ruiz, M., Sánchez-Pastor, P.S. and Romero, P.: Urban seismology: On the origin of earth  
789 vibrations within a city. *Scientific reports*, 7(1), 15296, 2017.
- 790 Dimitriu, R.G., Stanciu, I.M., Barbu M.-B., Dobrev, N., Dumitru, P.: First results on the western  
791 Black Sea coast geodynamics resulted from GeoPontica permanent GNSS stations network data

792 processing, in: Proceedings of the 17th International Multidisciplinary Scientific GeoConference  
793 SGEM, Albena, Bulgaria August 2017, 17(11), 149-157, 2017.

794 Dullaart, J.C., Muis, S., Bloemendaal, N. and Aerts, J.C.: Advancing global storm surge modelling  
795 using the new ERA5 climate reanalysis. *Climate Dynamics*, 54(1), 1007-1021, 2020.

796 Ebeling, C.W.: Inferring Ocean Storm Characteristics from Ambient Seismic Noise. A Historical  
797 Perspective, *Advances in Geophysics*, 53, 1-33. <https://doi.org/10.1016/B978-0-12-380938-4.00001-X>, 2012.

799 Enno, S.-E., Viticchie, B., Navia, D. and Grandell, J.: Meteosat-12 Lightning Imager: first year of  
800 observations and the main performance characteristics, in: 12th European Conference on Severe  
801 Storms, 08 August 2025, <https://doi.org/10.5194/ecss2025-152>, 2025.

802 Faranda, D., Messori, G., Coppola, E., Alberti, T., Vrac, M., Pons, F., Yiou, P., Saint Lu, M., Hisi,  
803 A. N. S., Brockmann, P., Dafis, S., Mengaldo, G., and Vautard, R.: ClimaMeter: contextualizing  
804 extreme weather in a changing climate, *Weather Climate Dynamics*, 5, 959-983,  
805 <https://doi.org/10.5194/wcd-5-959-2024>, 2024.

806 Floroiu, I., Anghel, A., Petrescu, L. and Datcu, M.: Clustering and Feature-Based Similarity  
807 Retrieval of Infrasound Events during Two Storms in Constanța, Romania, *International  
808 Conference on Machine Intelligence for GeoAnalytics and Remote Sensing (MIGARS)*, Bucharest,  
809 Romania, 2025, 1-4, <https://doi.org/10.1109/MIGARS67156.2025.11231952>, 2025.

810 Francoeur, J.W., Matoza, R.S., Ortiz, H.D. and De Negri, R.: Identification of transient seismo-  
811 acoustic signals from crashing ocean waves: template matching and location of discrete surf  
812 events. *Geophysical Journal International*, 243(2), ggaf317, 2025.

813 Garcés, M.A.: On infrasound standards, part 1 time, frequency, and energy scaling. *InfraMatics*,  
814 2(2),13–35, <https://doi.org/10.4236/inframatics.2013.22002>, 2013.

815 Gastmeier, W.J. and Howe, B.: Recent studies of infrasound from industrial sources. *Canadian  
816 Acoustics*, 36(3), 58-59, 2008.

817 Grafkina, M.V., Nyunin, B.N. and Sviridova, E.Y: Environmental monitoring and simulation of  
818 infrasound generating mechanism of traffic flow. *Journal of Ecological Engineering*, 20(7),  
819 2019.

820 Grevemeyer, I., Herber, R. and Essen, H.H.: Microseismological evidence for a changing wave  
821 climate in the northeast Atlantic Ocean. *Nature*, 408(6810), 349-352,  
822 <https://doi.org/10.1038/35042558>, 2000.

823 Groos, J.C. and Ritter, J.R.R.: Time domain classification and quantification of seismic noise in  
824 an urban environment. *Geophysical Journal International*, 179(2), pp.1213-1231, 2009.

- 825 Gualtieri, L., Camargo, S.J., Pascale, S., Pons, F.M.E., & Ekström, G.: The persistent signature of  
826 tropical cyclones in ambient seismic noise, *Earth and Planetary Science Letters*, 484, 287-294.  
827 <https://doi.org/10.1016/j.epsl.2017.12.026>, 2018.
- 828 Guerova, G., Jones, J., Douša, J., Dick, G., de Haan, S., Pottiaux, E., Bock, O., Pacione, R.,  
829 Elgered, G., Vedel, H. and Bender, M.: Review of the state of the art and future prospects of the  
830 ground-based GNSS meteorology in Europe, *Atmospheric Measurement Techniques*, 9(11),  
831 5385–5406, <https://doi.org/10.5194/amt-9-5385-2016>, 2016.
- 832 Herring, T., King, R., Floyd, M., McClusky, S.: GAMIT Reference Manual GPS Analysis at MIT  
833 Release 10.7. GAMIT/GLOBK, 2020.
- 834 Hersbach, H., Bell, B., Berrisford, P., Hirahara, S., Horányi, A., Muñoz-Sabater, J., Nicolas, J.,  
835 Peubey, C., Radu, R., Schepers, D. and Simmons, A.: The ERA5 global reanalysis, *Quarterly*  
836 *Journal of the Royal Meteorological Society*, 146(730), 1999-2049, 2020.
- 837 Hersbach, H., Bell, B., Berrisford, P., Biavati, G., Horányi, A., Muñoz Sabater, J., Nicolas, J.,  
838 Peubey, C., Radu, R., Rozum, I., Schepers, D., Simmons, A., Soci, C., Dee, D., Thépaut, J-N.:  
839 ERA5 hourly data on single levels from 1940 to present. Copernicus Climate Change Service  
840 (C3S) Climate Data Store (CDS), <https://doi.org/10.24381/cds.adbb2d47>, 2023.
- 841 Holmlund, K., Grandell, J., Schmetz, J., Stuhlmann, R., Bojkov, B., Munro, R., Lekouara, M.,  
842 Coppens, D., Viticchie, B., August, T. and Theodore, B.: Meteosat Third Generation (MTG):  
843 Continuation and innovation of observations from geostationary orbit, *Bulletin of the American*  
844 *Meteorological Society*, 102(5), E990-E1015, <https://doi.org/10.1175/BAMS-D-19-0304.1>, 2021.
- 845 Hua, J., Wu, M., Mulholland, J.P., Neelin, J.D., Tsai, V.C. and Trugman, D.T.: High-resolution  
846 precipitation monitoring with a dense seismic nodal array. *Scientific Reports*, 13(1), 11450,  
847 <https://doi.org/10.1038/s41598-023-38008-w>, 2023.
- 848 Hupe, P., Ceranna, L., Pilger, C., de Carlo, M., Le Pichon, A., Kaifler, B. and Rapp, M.: Assessing  
849 middle atmosphere weather models using infrasound detections from microbaroms. *Geophysical*  
850 *Journal International*, 216(3), 1761-1767, <https://doi.org/10.1093/gji/ggy520>, 2019.
- 851 Hupe, P., Ceranna, L., Le Pichon, A., Matoza, R.S. and Mialle, P.: International Monitoring  
852 System infrasound data products for atmospheric studies and civilian applications. *Earth System*  
853 *Science Data Discussions*, 14, 4201–4230, <https://doi.org/10.5194/essd-14-4201-2022>, 2022.
- 854 Iliescu, A. I., Rus, T., Danciu, V., Moldoveanu, C., & Ilie, A.: Current situation of GNSS networks  
855 in Romania, *Bulletin of University of Agricultural Sciences and Veterinary Medicine Cluj-Napoca.*  
856 *Horticulture*, 76(2), 2019.
- 857 Jakobsen, J.: Infrasound emission from wind turbines. *Journal of low frequency noise, vibration*  
858 *and active control*, 24(3), 145-155, 2005.

859 Jiao, D., Xu, N., Yang, F. and Xu, K.: Evaluation of spatial-temporal variation performance of  
860 ERA5 precipitation data in China. *Scientific Reports*, 11(1), 17956, 2021.

861 Johnston, G., Riddell, A. and Hausler, G.: The international GNSS service, in: Springer handbook  
862 of global navigation satellite systems, edited by: Teunissen, P.J. and Montenbruck, O., Springer,  
863 Cham, Switzerland, 967-982, [https://doi.org/10.1007/978-3-319-42928-1\\_33](https://doi.org/10.1007/978-3-319-42928-1_33), 2017.

864 Jones, J., Guerova, G., Douša, J., Dick, G., de Haan, S., Pottiaux, E., Bock, O., Pacione, R. and  
865 Van Malderen, R.: Advanced GNSS tropospheric products for monitoring severe weather events  
866 and climate, COST Action ES1206 Final Action Dissemination Report, 563, 2020.

867 Karabatić, A., Weber, R. and Haiden, T.: Near real-time estimation of tropospheric water vapour  
868 content from ground based GNSS data and its potential contribution to weather now-casting in  
869 Austria, *Advances in Space Research*, 47(10), 1691–1703,  
870 <https://doi.org/10.1016/j.asr.2010.10.028>, 2011.

871 Kober, K. and Tafferner, A.: Tracking and nowcasting of convective cells using remote sensing  
872 data from radar and satellite, *Meteorologische Zeitschrift*, 1(18), 75-84,  
873 <https://doi.org/10.1127/0941-2948/2009/359>, 2009.

874 Koper, K.D. & Burlacu, R.: The fine structure of double-frequency microseisms recorded by  
875 seismometers in North America. *Journal of Geophysical Research: Solid Earth*, 120(3), 1677-  
876 1691. <https://doi.org/10.1002/2014JB011820>, 2015.

877 Kokou, P.: Status of the MTG-II Lightning Imager commissioning activities, in: EUMETSAT  
878 Conference 2023, 1-C GEO – MTG, Malmö, Sweden, 12 September 2023, 2023.

879 Landès, M., Ceranna, L., Le Pichon, A. and Matoza, R.S.: Localization of microbarom sources  
880 using the IMS infrasound network. *Journal of Geophysical Research: Atmospheres*, 117(D6),  
881 <https://doi.org/10.1029/2011JD016684>, 2012.

882 Landskron, D., Böhm, J.: VMF3/GPT3: refined discrete and empirical troposphere mapping  
883 functions, *Journal of Geodesy*, 92, 349–360, <https://doi.org/10.1007/s00190-017-1066-2>, 2018.

884 Li, L., Boué, P., Retailleau, L., & Campillo, M.: Spatiotemporal Correlation Analysis of Noise-  
885 Derived Seismic Body Waves With Ocean Wave Climate and Microseism Sources, *Geochemistry,*  
886 *Geophysics, Geosystems*, 21(9), <https://doi.org/10.1029/2020GC009112>, 2020.

887 Listowski, C., Forestier, E., Dafis, S., Farges, T., De Carlo, M., Grimaldi, F., Le Pichon, A.,  
888 Vergoz, J., Heinrich, P. and Claud, C.: Remote monitoring of Mediterranean hurricanes using  
889 infrasound, *Remote Sensing*, 14(23), 6162, <https://doi.org/10.3390/rs14236162>, 2022.

890 MacQueen, J.: Some methods for classification and analysis of multivariate observations, in:  
891 Proceedings of the Fifth Berkeley Symposium on Mathematical Statistics and Probability,  
892 Berkeley, California, January 1967, 5, 281-298, 1967.

893 Marut, G., Hadas, T., Kaplon, J., Trzcina, E. and Rohm, W.: Monitoring the water vapor content  
894 at high spatio-temporal resolution using a network of low-cost multi-GNSS receivers, *IEEE*  
895 *Transactions on Geoscience and Remote Sensing*, 60, 1-14,  
896 <https://doi.org/10.1109/TGRS.2022.3226631>, 2022.

897 Pásztor, M., Czanik, C. and Bondár, I.: A single array approach for infrasound signal  
898 discrimination from quarry blasts via machine learning, *Remote Sensing*, 15(6), 1657,  
899 <https://doi.org/10.3390/rs15061657>, 2023.

900 Le Pichon, A., Matoza, R., Brachet, N. and Cansi, Y.: Recent enhancements of the PMCC  
901 infrasound signal detector. *Inframatics*, 26, 5-8, 2010.

902 Price, I., Sanchez-Gonzalez, A., Alet, F., Andersson, T.R., El-Kadi, A., Masters, D., Ewalds, T.,  
903 Stott, J., Mohamed, S., Battaglia, P. and Lam, R.: Probabilistic weather forecasting with machine  
904 learning. *Nature*, 637(8044), 84-90, 2025

905 Priego, E., Jones, J., Porres, M.J. and Seco, A.: Monitoring water vapour with GNSS during a  
906 heavy rainfall event in the Spanish Mediterranean area, *Geomatics, Natural Hazards and Risk*,  
907 8(2), 282–294, <https://doi.org/10.1080/19475705.2016.1201150>, 2017.

908 Retailleau, L. & Gualtieri, L.: Multi-phase seismic source imprint of tropical cyclones, *Nature*  
909 *Communications*, 12(1), <https://doi.org/10.1038/s41467-021-22231-y>, 2021.

910 Rindraharisaona, E.J., Réchou, A., Fontaine, F.R., Barruol, G., Stamenoff, P., Boudevillain, B.,  
911 Rigaud-Louise, F. and Delcher, E.: Seismic signature of rain and wind inferred from seismic data,  
912 *Earth and Space Science*, 9(10), p.e2022EA002328, 2022.

913 Šindelářová, J., Chum, J., Skripnikova, K., and Base, J.: Atmospheric infrasound observed during  
914 intense convective storms on 9–10 July 2011, *Journal of Atmospheric and Solar-Terrestrial*  
915 *Physics*, 122, 66–74, <https://doi.org/10.1016/j.jastp.2014.10.014>, 2015.

916 Šindelářová, T., De Carlo, M., Czanik, C., Ghica, D., Kozubek, M., Podolská, K., Baše, J., Chum,  
917 J., and Mitterbauer, U.: Infrasound signature of the post-tropical storm Ophelia at the Central and  
918 Eastern European Infrasound Network, *Journal of Atmospheric and Solar-Terrestrial Physics*, 217,  
919 105603, <https://doi.org/10.1016/j.jastp.2021.105603>, 2021.

920 Smirnov, A., De Carlo, M., Le Pichon, A., Shapiro, N.M. and Kulichkov, S.: Characterizing the  
921 oceanic ambient noise as recorded by the dense seismo-acoustic Kazakh network. *Solid Earth*,  
922 12(2), 503-520, 2021.

923 Soci, C., Hersbach, H., Simmons, A., Poli, P., Bell, B., Berrisford, P., Horányi, A., Muñoz-Sabater,  
924 J., Nicolas, J., Radu, R. and Schepers: The ERA5 global reanalysis from 1940 to 2022. *Quarterly*  
925 *Journal of the Royal Meteorological Society*, 150(764), 4014-4048, 2024.

- 926 Sokol, Z., Szturc, J., Orellana-Alvear, J., Popova, J., Jurczyk, A. and Célleri, R.: The role of  
927 weather radar in rainfall estimation and its application in meteorological and hydrological  
928 modelling—A review, *Remote Sensing*, 13(3), 351, 2021.
- 929 Stopa, J.E., Cheung, K.F., Garcés, M.A. and Badger, N.: Atmospheric infrasound from nonlinear  
930 wave interactions during Hurricanes Felicia and Neki of 2009, *Journal of Geophysical Research:*  
931 *Oceans*, 117(C12), <https://doi.org/10.1029/2012JC008257>, 2012
- 932 Stott, P.: How climate change affects extreme weather events. *Science*, 352(6293), 1517-1518,  
933 <https://doi.org/10.1126/science.aaf7271>, 2016.
- 934 Tanimoto, T. & Anderson, A.: Seismic noise between 0.003 Hz and 1.0 Hz and its classification,  
935 *Progress in Earth and Planetary Science*, 10(1), <https://doi.org/10.1186/s40645-023-00587-7>,  
936 2023.
- 937 Taweesintananon, K., Landrø, M., Potter, J.R., Johansen, S.E., Rørstadbotnen, R.A., Bouffaut, L.,  
938 Kriesell, H.J., Brenne, J.K., Haukanes, A., Schjelderup, O. and Storvik, F.: Distributed acoustic  
939 sensing of ocean-bottom seismo-acoustics and distant storms: A case study from Svalbard,  
940 Norway. *Geophysics*, 88(3), B135-B150, 2023.
- 941 Tiberia, A., Mascitelli, A., D’adderio, L.P., Federico, S., Marisaldi, M., Porcù, F., Realini, E.,  
942 Gatti, A., Ursi, A., Fuschino, F. and Tavani, M.: Time evolution of storms producing terrestrial  
943 gamma-ray flashes using ERA5 reanalysis data, GPS, lightning and geostationary satellite  
944 observations. *Remote Sensing*, 13(4), 784, 2021.
- 945 Vaquero-Martínez, J. and Antón, M.: Review on the role of GNSS meteorology in monitoring  
946 water vapor for atmospheric physics, *Remote Sensing*, 13(12), 2287,  
947 <https://doi.org/10.3390/rs13122287>, 2021.
- 948 Viticchie, B., Lekouara, M., Hungershofer, K., Joro, S., Grandell, J., Maufrais, A., Marquez, M.J.,  
949 Munro, R.: Algorithm Theoretical Basis Document (ATBD) for L2 processing of the MTG  
950 Lightning Imager data, Rapp. Tech. EUMESTAT, 6, 2020.
- 951 Waxler, R., Frazier, W. G., Talmadge, C. L., Liang, B., Hetzer, C., Buchanan, H., and Audette, W.  
952 E.: Analysis of infrasound array data from tornadic storms in the southeastern United States,  
953 *Journal of the Acoustical Society of America*, 156, 1903–1919,  
954 <https://doi.org/10.1121/10.0028815>, 2024.
- 955 Wessel, P., Luis, J.F., Uieda, L.A., Scharroo, R., Wobbe, F., Smith, W.H. and Tian, D.: The generic  
956 mapping tools version 6, *Geochemistry, Geophysics, Geosystems*, 20(11), 5556-5564,  
957 <https://doi.org/10.1029/2019GC008515>, 2019.
- 958 Wilgan, K., Rohm, W. and Bosy, J.: Multi-observation meteorological and GNSS data comparison  
959 with numerical weather prediction model, *Atmospheric Research*, 156, 29–42,  
960 <https://doi.org/10.1016/j.atmosres.2014.12.011>, 2015.

961 Wu, G., Qin, S., Mao, Y., Ma, Z. and Shi, C.: Validation of precipitation events in ERA5 to gauge  
962 observations during warm seasons over eastern China. *Journal of Hydrometeorology*, 23(5), 807-  
963 822, 2022.  
964